Topics in Neutron Star Physics

A Dissertation

Presented to the Faculty of the Graduate School

of Cornell University

in Partial Fulfillment of the Requirements for the Degree of

Doctor of Philosophy

by

Katherine Elena Henriksson

January 2015

TOPICS IN NEUTRON STAR PHYSICS

Katherine Elena Henriksson, Ph.D.

Cornell University 2015

We present here results from two independent studies of neutron star physics. In chapter 2, we examine the detailed structure of the poloidal magnetic fields of a neutron star with a strong type II superconducting core and a normal crust. The star is modeled as an axisymmetric configuration in hydrodynamic equilibrium in Newtonian gravity. We assume that the equation of state is barotropic. In the strong type II limit, the core magnetic field is a function of density alone: $H = H(\rho)$. This peculiarity enables us to solve for the shapes of the field lines. We consider the case of field lines from the core hitting the crust boundary vertically, and we show that while they may not penetrate far into the normal crust, they nevertheless set the scale for the magnitude of the external field. Intriguingly, we find that for this configuration the external field is around $B \sim 10^{12}\,\mathrm{G}$, which is typical for a radiopulsar. It is quite remarkable that this result is entirely a function of the microphysics at the core–crust boundary. In chapter 3, we present work in finding a solution to Einstein's equations describing a black hole–neutron star binary inspiral close to merger. We consider the case of a 6:1 mass ratio system with a star governed by a polytropic $\Gamma = 2$, SLy, or LS220 equation of state. The star is assumed to be irrotational and in a quasiequilibrium orbit. We present the numerical techniques that we have used in order to improve the convergence of methods for obtaining solutions describing such systems. We obtain solutions for a polytropic star of compactness $M/R \leq 0.21$, for an SLy star with $M/R \leq 0.25$, and for a LS220 star with $M/R \leq 0.26$. These compactness values are significantly higher than any previously published results. The highest compactness star has mass $2\,\mathrm{M}_\odot$, corresponding to the highest reliably measured neutron star mass.

Biographical Sketch

Katherine was born and raised in the San Francisco Bay Area, where she attended primary and secondary school. She attended the University of California, Berkeley for her undergraduate degree, where she majored in Physics and Mathematics. She received multiple scholarships from the Department of Physics, served as an undergraduate student instructor for the Department of Mathematics, and was inducted into the Phi Beta Kappa and Golden Key International honor societies. She graduated in 2008 with a Bachelor of Arts with High Distinction.

She began her studies at Cornell University with an interest in theoretical high energy physics, but soon shifted to studying astrophysical theory through numerical and analytic calculations. Katherine received a NASA/New York Space Grant Consortium fellowship in 2012. She has volunteered with different groups, including the Expanding Your Horizons conference, which encourages interest in math and science in middle-school aged girls. She received her Master of Science degree from Cornell in January 2012.

This thesis is dedicated to all those who have helped me get to where I am today.

Acknowledgements

I am indebted to my advisors, Ira Wasserman and Saul Teukolsky, for their help through my graduate career. Their insight, encouragement, and advice has been invaluable in the research that I have performed under them, and their guidance has helped prepare me to be effective in working independently on serious problems.

I am grateful for the support and camaraderie of my colleagues, Andy Bohn, François Hébert, Dan Hemberger, Curran Muhlberger, and William Throwe, who were always fun to be around. Their constant company in the office, at events like game nights, and online made my time at Cornell very enjoyable.

I also want to thank my family, without whose love and support I could not have done this. Even though I was very far from them, they were always just a phone call away to cheer me up or just sit and chat about my day or the Ithaca weather, which is very different from California weather.

This research has been supported in part by NSF grants AST-0606710, PHY-1125915, PHY-1306125, and AST-1333129, by a fellowship from the NASA/New York Space Grant Consortium, by the College of Arts and Sciences, Cornell University, and by a grant from the Sherman Fairchild Foundation. The research was performed in part using the Zwicky computer system operated by the Caltech Center for Advanced Computing Research and funded by NSF MRI No. PHY-0960291 and the Sherman Fairchild Foundation.

Table of Contents

Biographical Sketch . . . iii
Dedication . . . iv
Acknowledgements . . . v
Table of Contents . . . vi
List of Figures . . . viii
List of Tables . . . ix

1 Introduction **1**
1.1 Poloidal Magnetic Fields in Superconducting Neutron Stars . . . 2
1.1.1 Field in Superconducting Core . . . 4
1.1.2 Field in Normal Region and Transition . . . 5
1.1.3 Discussion . . . 6
1.2 Binary Black Hole–Compact Neutron Star Initial Data . . . 6
1.2.1 Solution Method . . . 8
1.2.2 Relaxation . . . 11
1.2.3 Momentum Control . . . 12
1.2.4 Discussion . . . 12

2 Poloidal Magnetic Fields In Superconducting Neutron Stars **15**
2.1 Introduction . . . 16
2.2 Overview . . . 19
2.2.1 Requirements of Hydrostatic Balance . . . 21
2.2.2 Field Configuration in the Type II Core . . . 22
2.2.3 Solution in the Normal Shell . . . 25
2.2.4 Magnetic Distortions Due to Poloidal Fields . . . 31
2.3 Toy Model: Vertical Field in the Core . . . 34
2.4 Numerical Solutions . . . 36
2.4.1 Field Line Structure . . . 36
2.4.2 Magnetic Distortion: Mass Quadrupole Moment . . . 39
2.4.3 Perturbative Corrections: Nonzero ℓ and β . . . 40
2.5 Discussion and Conclusions . . . 41
2.A Perturbation Solutions . . . 46
2.A.1 Surface Currents from Transition Layer . . . 47

2.A.2 Field Lines Poking in from the Core 48
2.B The Thin Shell Approximation for the Transition Layer 51

3 Initial data for high-compactness black hole–neutron star binaries 53
3.1 Introduction 54
3.2 Methods 58
3.2.1 Neutron Star Surface Adjustment 59
3.2.2 ADM Momentum Control 62
3.3 Results 65
3.3.1 Polytropic $\Gamma = 2$ EOS 65
3.3.2 SLy EOS 66
3.3.3 LS220 EOS 68
3.4 Conclusions 71

Bibliography 75

List of Figures

2.1 Field line configurations in the Type II superconducting core 26
2.2 Magnetic field components in the normal shell 31
2.3 Field line configurations for different models of the Type II core 37
2.4 Field line configuration with nonzero core boundary B field strength 39

3.1 The domain used for the binary black hole–neutron star system 60
3.2 Spectral convergence for a polytropic family of BHNS configurations 67
3.3 Spectral convergence for an SLy family of BHNS configurations 69
3.4 Spectral convergence for an LS220 family of BHNS configurations 72

List of Tables

2.1 Current parameters and multipoles in finite transition thickness solution . . 41

3.1 Solved quantities for a polytropic family of BHNS configurations 68
3.2 Solved quantities for an SLy family of BHNS configurations 70
3.3 Solved quantities for an LS220 family of BHNS configurations 71

1 Introduction

Neutron stars provide an especially interesting subject of study because of their rather exotic physics. One the one hand, their properties as condensed matter objects are quite extreme. Typical surface magnetic fields are around $10^{12}\,\mathrm{G}$, and when such a star rotates, it may emit very regular pulses of electromagnetic radiation. Neutron stars are also the densest known macroscopic objects in the universe, with densities exceeding $3 \times 10^{14}\,\mathrm{g\,cm^{-3}}$, the density of an atomic nucleus. At such extreme densities, the star is primarily composed of degenerate interacting baryons, leading to pressures sufficient for hydrostatic balance for stellar masses up to at least $2\,\mathrm{M}_\odot$. The core of the star becomes so dense that nearly all of the matter forms neutrons, the more stable hadron at these pressures. The neutrons form a superfluid core, with the remaining protons dissolved in the core and forming a type II superconductor. This superconductor does not exhibit the Meissner effect, and thus magnetic fields $\sim 10^{14}$–$10^{16}\,\mathrm{G}$ are allowed in the core. Understanding the particular shape of the core fields allows better analyses of the field everywhere and also the resulting distortion to the star.

On the other hand, the incredible density of neutron stars combined with their size results in a highly extreme gravitational field in the neighborhood of the stars. The Schwarzschild radius of a neutron star is a few tenths of the neutron star radius, and thus inside the neutron star and in its vicinity the distortion of the surrounding space-time is appreciable. If we have a neutron star in a binary system with a black hole, the motion of these objects in their orbit as they near merger produces $\sim 0.1\,\mathrm{kHz}$ gravitational radiation, which we hope to detect directly. A quantitative prediction of the radiation produced is required in order to detect it,

and a complete solution for the spacetime in the vicinity of the two objects close to merger is a necessary aspect of this.

In this dissertation, we examine two separate aspects of neutron star physics: the shape of neutron star magnetic field lines in and around its superconducting core, and the spacetime metric and matter density in a region where a compact neutron star–black hole binary is close to merger. In the rest of this chapter, we give a brief introduction to both of these topics.

1.1 Poloidal Magnetic Fields in Superconducting Neutron Stars

The theory of superconductivity in nuclear matter was first applied to neutron stars in Baym *et al.* [1]; the stars are commonly around 10^8 K, whereas the the critical temperature of protons in their cores is 10^9–10^{10} K, and so they are in a superconducting regime. The specific behavior of the core is governed by the relative sizes of the proton coherence length ξ_p and the London length λ_L [2]. In particular, it is found that when $\lambda_L > \xi_p/\sqrt{2}$ the core will form a type II superconductor, wherein magnetic fields are not excluded from the matter but rather are confined to flux tubes each carrying a flux quantum $\Phi_0 = \pi\hbar c/e$ of magnetic flux. Outside the core of the flux tube, the strength of the magnetic field decays exponentially with a scale λ_L. The particular value of ξ_p, important for this analysis, is still somewhat uncertain, with values still being refined [3, 4], but it is likely that for baryon densities less than about twice nuclear density, a type II superconductor will result.

Two recent observations are relevant to the topic of neutron star superconductivity. The first is the X-ray observations of the cooling Cassiopeia A supernova remnant. Measurements of the cooling rate of the neutron star remnant show that it is cooling primarily via Cooper pair formation in the neutron superfluid. Without proton superconductivity, the URCA and

modified URCA processes would lead to faster cooling, but these are suppressed when the protons are bound into Cooper pairs [5–7]. The second important observation was the recent discovery of a $2\,\mathrm{M}_\odot$ neutron star, which constrains the available neutron star equations of state and makes it likely that the core could not far exceed twice nuclear density [8]. Both these observations support theoretical reasoning for type II proton superconductivity in neutron star cores.

Given these results, it is important to be able to precisely model the effect the superconductor has on the star as a whole. Previous analyses have considered a purely normal star with no superconducting core [9], poloidal fields of a uniform density star [10], and toroidal fields in a Newtonian $\Gamma = 2$ polytrope [11–13]. Here we consider the case of poloidal fields in an axisymmetric Newtonian $\Gamma = 2$ polytrope, fully accounting for the effects of the superconducting core on the star. The most important result we obtain is the prediction of $B \sim 10^{12}\,\mathrm{G}$ at the surface of the star, in agreement with the value commonly observed astrophysically. It is of note that this result is only a consequence of microscopic physics of the superconductor and of reasonable assumptions about the general shape of the fields, without requiring any astrophysically based inputs.

In this work, we obtain an equilibrium solution to the star, following the requirements of hydrostatic balance. We use a perturbative approach, in which the magnetic stress is assumed to have only a small effect on the background configuration. In this way, the magnetic field configuration can be obtained using the unperturbed background density, with corrections to the fields due to the perturbed density arising only at second order. A complication arises because of the complex behavior at the boundary of the core and the normal crust, which we treat with the application of an appropriate boundary condition.

We now sketch how the solution is obtained; details are given in chapter 2.

1.1.1 Field in Superconducting Core

In the core, we assume that we are in the strong type II limit, so that $B \ll H$ and we can ignore the interactions between field lines. We also assume that the free energy has no dependence on the direction of $\mathbf{B}$, only its magnitude, i.e. that there are no preferred directions, and this implies that $\mathbf{H} = H_{c1}(\rho)\hat{\mathbf{B}}$. The magnitude of $\mathbf{H}$ here is given by $H_{c1}(\rho)$, the first superconducting critical field strength, which is only a function of density, and so the problem therefore reduces to the question of finding the direction of the field everywhere. Directly solving Maxwell's equation for $\mathbf{H}$, however, is complicated, even if we were to know the current density somehow. Instead, we can concentrate on solving for the shape of a single field line. We can parameterize a given field line by its arclength, and use this to define various quantities describing the shape of the field line. Using these definitions, Maxwell's equation for $\mathbf{H}$ can be transformed into (2.12) and then into (2.16), which we can integrate numerically to find the shape of the field line.

It is worth mentioning here a couple relevant aspects of this physical system. There is a quantity which we call A that is constant along magnetic field lines, and in that sense serves to label each line. This property holds generally for poloidal fields. Furthermore, hydrostatic balance requires that $\frac{J}{\rho r \sin\theta}$ is constant along field lines, which gives us the quantity $\mathcal{J}(A)$ appearing in (2.12) and (2.16).

Given a background solution to provide ρ, input from microphysics for the form of $H(\rho)$, and a value for $\mathcal{J}(A)$, we can determine the shape of the field line. The line must pass through the equator vertically, and so if a condition is provided for the other end of the field line where it passes into the normal crust, it is possible to determine numerically the value of $\mathcal{J}(A)$ (if any) that satisfies this condition for a line with a given radius at the equator. In this investigation, we use the condition that field lines must meet the boundary with the normal core vertically, which we expect to yield the field configuration making the external

field the most dipolar.

1.1.2 Field in Normal Region and Transition

In the normal crust, we have simply that $\mathbf{H} = \mathbf{B}$, and so Maxwell's equation for $\mathbf{H}$ becomes a partial differential equation for A that we can solve directly provided that we know $\mathcal{J}(A)$. The principal difficulty comes in determining this function consistently with the core and the external vacuum region solutions; continuity at the crust–core and surface boundaries provides the main constraint on the dipole field in the crust. The boundary layer between the superconducting core and the normal crust exhibits quite complicated physics, and it is the treatment of this layer that drives two separate cases we can consider.

In the first case, we consider the transition region to be of zero thickness. In this situation, we can find that the current parameter $\mathcal{J}(A)$ driving the fields in the normal region is simply a constant for all the field lines in the crust. When $B \to 0$ at the boundary, the field lines from the core do not penetrate into the normal shell at all, but continuity there still enables the core field strength to influence fields in the crust. The key result we find is that at the stellar surface,

$$B \sim H_b \left(1 - \frac{r_b}{R}\right) \tag{1.1}$$

where H_b and r_b are the magnetic field and radius at the crust–core boundary, respectively. Given typical characteristic values, this yields $B \sim 10^{12}$–$10^{13}\,\mathrm{G}$. Both r_b and H_b can be deduced from microphysics, so that this is a fairly interesting result, as it agrees with astrophysical measurements for many pulsars.

The second case is that of a transition region of finite thickness. If it can still be considered thin, it can be treated as a surface current in the boundary. This case introduces a considerable amount of complication into the solution procedure. Notably, it results in a non-constant value for $\mathcal{J}(A)$, and creates non-dipolar fields in the shell and the external

vacuum, which can be solved perturbatively.

1.1.3 Discussion

Given the fields determined inside the star, we can solve the equations of hydrostatic balance to enforce equilibrium among forces from pressure, gravity, and magnetism. We can use this to obtain the multipole moments of the star, and in particular the quadrupole moment, which holds some astrophysical relevance. We write the quadrupole term in the expansion of the gravitational potential evaluated at the surface, which is a related quantity, as $-\mathcal{M}_2 \times GM/R$. With typical values for a neutron star we find $\mathcal{M}_2 \sim 10^{-9}$, which is fairly small but could potentially be detectable.

One interesting result of this analysis is the determination of a characteristic 10^{12} G field at the star surface. A number of stars have been found with fields differing significantly from this prediction, and so we note a number of simplifying assumptions that could affect this. We only considered a particular form for the core field lines where they hit the boundary vertically; other boundary conditions at the transition region could affect this result. Furthermore, the strong type II limit could break down, with $B \sim H$ in the core; this would likely be the case for magnetars. Toroidal magnetic fields were also not discussed, and could have an effect on the results here. However, many stars have been observed with the value discussed herein, and this analysis provides an explanation for their field strengths.

1.2 Binary Black Hole–Compact Neutron Star Initial Data

The subject of numerical relativity is a very rich one, and finds particular prominence thanks to large experiments such as LIGO and VIRGO. These experiments seek to obtain the first direct detection of gravitational radiation, predicted by general relativity, as well as provide observations of events such as binary black hole mergers, which provide no other means of observation. Such observations could be very useful in constraining models of

stellar evolution by determining the frequency with which such events occur in our local neighborhood of the universe. Actually detecting gravitational waves is an exceptionally challenging task however, because of the weakness of such a signal. In its core frequency band near 100 Hz, Advanced LIGO is expected to be able to detect strains $h \gtrsim 3 \times 10^{-24} / \sqrt{\text{Hz}}$ [14], which are incredibly small. A naïve search would have great difficulty finding such a signal, but using matched filtering techniques based on the known signal that should be detected, such a problem becomes tractable. Numerical relativity is crucial in providing and calibrating the waveforms to use for this detection.

While Einstein's equations remain unsolvable analytically except in a few special cases, numerical techniques offer the opportunity to obtain precise solutions for binary mergers. Large scientific codebases such as the Spectral Einstein Code (SpEC) contain routines to calculate the initial configuration for a binary system and the evolution of that system through merger and ringdown, obtaining the gravitational waveforms the system would produce. In addition to binary black hole mergers, black hole–neutron star mergers and binary neutron star mergers are also of interest. In particular, it is expected that there would be around five times more BHNS mergers than BBH mergers occurring in a region of space per year, and as many as 30 times more NSNS than BHNS mergers [15].

Numerical simulations for binary black hole systems first became feasible with the work of Pretorius [16]. Since then, a large number of groups have carried out simulations. For a review and further references, see [17]. A number of studies of binary neutron star systems have also been performed [for a review, see 18, 19], based on work from Teukolsky [20] and Shibata [21]. The majority of this work uses finite difference methods. The use of spectral methods started in computational fluid dynamics in the 1970's, and these methods were first applied to the initial value problem for black hole binary systems by Grandclément *et al.* [22]. Essential to the problem of initial data is a way to solve the elliptic equations that arise from Einstein's equations, and our work in particular is based on the general multi-

domain elliptic solver by Pfeiffer *et al.* [23]. Using a technique similar to that described in [24] for approaching the solution of the neutron star, Foucart *et al.* [25] were able to obtain solutions for various binary black hole–neutron star systems. Their solver forms the basis of our approach.

In chapter 3, we consider the problem of simulating a black hole–neutron star binary during inspiral, near merger. In particular, we would like to obtain a self-consistent solution ("initial data") to the relevant Einstein equations at a single initial time, so that that solution can be evolved forward in time to obtain the complete waveform. The method developed in [25] works well for the case of a binary where the neutron star is of low to moderate compactness. Here, we develop a method that can solve for systems where the compactness is moderate to high. We use the same infrastructure they used, which is part of the Spectral Einstein Code (SpEC) software, in order to extend it to support higher compactnesses than previously.

1.2.1 Solution Method

Fundamentally, this is a problem of solving a system of nonlinear elliptic partial differential equations. There are a rich variety of methods one can use to solve such a system; we rely upon the Spectral Elliptic Solver (Spells) routine introduced by Pfeiffer *et al.* [23], which forms the basis of the SpEC BHNS initial data solver. At each point of the simulation grid, an approximation is made for the derivatives, and the elliptic equations and boundary conditions are transformed to a large system of nonlinear algebraic (rather than differential) equations. This system is then solved with the aid of the PETSc scientific library. The particular prescription followed for approximating the derivatives is the pseudo-spectral one; for details on this prescription see [26, sec. 20.7], as well as [27, chap. 7] and [28–30].

In order to solve this system in practice, an iterative approach is used. Various conditions such as vanishing center-of-mass momentum, specified black hole spin, and the quasi-

equilibrium condition that the objects should be approximately stationary in the corotating frame impose certain restrictions, which allows solving for free parameters such as the location of the black hole center or the orbital angular velocity. The bulk of the computational cost is in solving the elliptic equations and boundary conditions for the metric and the velocity potential. At each step of the iterative procedure, each quantity has its new value determined sequentially by solving its equation without modifying the other quantities. By choosing an analytic approximate initial guess and iterating these steps, a solution for all of the relevant parameters, and thus the system as a whole, should be found.

In practice, this procedure works well for a large class of physically interesting systems. A test case we use is that of a nearly circular 6:1 mass ratio (black hole/neutron star) inspiral of a $1.4\,\mathrm{M}_\odot$ neutron star and a non-spinning black hole. The objects are taken to be 8 times the black hole's Schwarzschild radius apart, and the neutron star equation of state is taken as a $\Gamma = 2$ polytrope. The above procedure works well for this system when the compactness $\mathcal{C} \equiv M/R$ of the neutron star is around 0.15, but as that value is increased to 0.2 and higher, the iterations of the SpEC solver fail to converge and we are unable to obtain a solution. If we consider an alternative more physically reasonable SLy equation of state, the trouble happens even sooner, for compactness of only 0.17. Our goal then is to search for techniques that would allow finding solutions with higher compactness. Note that for the family of polytropic equations of state we consider, an isolated neutron star would be stable up to a compactness of approximately 0.21. With an SLy equation of state, it remains stable up to a compactness of about 0.3.

A few different techniques can be tried in order to obtain compact solutions. We found that among the various methods we attempted, two in particular enabled us to obtain the desired solutions. The first is a modification of how we update variables after solving the equation that governs them. Rather than using the new value directly, the new value can be combined with the old, to reduce the magnitude of the change. Such a prescription is known

as relaxation. The second was to change how we accommodate linear ADM momentum drift that creeps into the system. The method of [25] is to adjust the position of the black hole to drive the momentum toward zero. Instead, we introduce a boost to the boundary conditions imposed at infinity. The strength of the boost is also adjusted using the method of relaxation, to ensure it does not change too abruptly during the solution method. These two methods were found to be sufficient to allow solving for compact systems, corresponding to stars of mass up to $2\,M_\odot$.

Domain

An important aspect of the solver is the domain that is used to solve the equations. The domain must be well-matched to the problem. A number of subdomains are used to cover the domain of interest, either overlapping or just touching at their boundaries. If a region of the domain has insufficient resolution to resolve behavior within it, the solution may suffer, and if it has excessive resolution it will be computationally wasteful. Therefore, it is important to be able to tune the concentration of resolution, and multiple subdomains provide the easiest means. Furthermore, with a neutron star contained in the domain, a discontinuity in the derivatives of physical quantities exists at the surface of the star, and having such a feature in the middle of a spectral subdomain would result in Gibbs phenomenon, ruining spectral convergence. Therefore, it is imperative to be able to ensure that such a discontinuity lies on the boundary of a subdomain. It is also desirable to make the apparent horizon of the black hole coincide with a subdomain boundary so as to enforce appropriate boundary conditions there. One of the steps of the iteration is to update the domain with this information, as the elliptic solve modifies the locations of these features.

The domain we use in this solver is that described in [25], which consists of the union of several subdomains in the shape of parallelepipeds, spherical shells, and cylindrical shells. The size, location, and resolution of each subdomain is chosen in order to provide adequate

coverage in resolution for relevant regions, without requiring high resolution everywhere. The entire domain is shown and further described in figure 3.1.

1.2.2 Relaxation

For some of the quantities appearing in the solution, their value does not change significantly during the procedure, and so relaxation is not needed. However, others such as the metric and matter variables are much more prone to lead to difficulty for the solution. The position of the neutron star surface is another such quantity. We define a relaxation parameter λ through the scheme

$$u_{\text{new}} = \lambda u^* + (1 - \lambda) u_{\text{old}} \tag{1.2}$$

for obtaining the new value of a quantity from its old value and its solved value u^*. Using $\lambda = 1$ corresponds to a simple update with no relaxation. A typical value used in the SpEC solver and necessary even at low compactness is $\lambda = 0.3$. Using this value with relaxation applied only to the metric quantities and velocity potential allows obtaining solutions for compactnesses up to 0.18 with the polytropic equation of state. To reach higher values we can choose a lower λ: with λ as low as 0.15, solutions could be obtained for $\mathcal{C} \lesssim 0.2$.

For the more physically realistic SLy equation of state, this procedure still did not enable obtaining a solution above $\mathcal{C} \approx 0.16$. However, another quantity that we had not previously considered for relaxation is the computed location of the neutron star surface. The location of the surface is used to define the boundary of the subdomain containing the star, and that location is important because if the subdomain boundary does not coincide with the actual surface, the discontinuity present there will severely degrade performance of the solution method. We introduced a relaxation procedure for the coefficients defining the surface and found that solutions for the SLy equation of state could now be found for $\mathcal{C} \lesssim 0.19$, much better than previously. Thus this approach provides solutions for higher compactness than

previously accessible, although it still encounters trouble for high enough compactness.

For further details on this scheme, refer to section 3.2.1.

1.2.3 Momentum Control

One method of adjusting the linear ADM momentum in this system is simply to move the black hole. This is because of the various constraints that are imposed elsewhere, such as the requirement that the center of momentum remain fixed. That requirement is satisfied by modifying the black hole momentum when its center is moved, which thus feeds back into the total momentum. The method of [25] achieves this by approximating the system as Newtonian. From the current value of the total ADM momentum it is possible to predict the change in the black hole center that will result in the momentum reaching zero. Such a scheme is fairly effective for less compact binaries, but we found that the jumps induced in the black hole position inevitably caused convergence failure for systems with a compact neutron star.

An alternative scheme, which we found to be effective even with compact stars, is to apply boosted boundary conditions at the outer boundary of the domain while keeping the black hole center fixed. Generally speaking, this tends to introduce a drift in the coordinate location of the center of mass, which the above does not, but the former method does not allow very compact solutions to be obtained.

For additional details about this method, see section 3.2.2.

1.2.4 Discussion

By applying the two techniques discussed above, large improvements were made in our ability to solve for BHNS initial data with a compact neutron star. Combining these two methods allowed us to obtain compact BHNS solutions with a variety of equations of state. For a $\Gamma = 2$ polytrope, we could obtain solutions with $\mathcal{C} = 0.21$ and $M_{\rm NS} = 1.4\,{\rm M}_\odot$, the highest stable

compactness for this family of equations of state. For the SLy and LS220 equations of state, we could find solutions where the neutron star mass is $1.9\,M_\odot$ and $2\,M_\odot$, respectively, with the latter being the highest mass (and most compact star) to have been reliably measured. We thus consider these methods to successfully allow solutions for compact stars. These results are discussed further in section 3.3.

2 | Poloidal Magnetic Fields In Superconducting Neutron Stars[1]

Abstract

We develop the formalism for computing the magnetic field within an axisymmetric neutron star with a strong Type II superconductor core surrounded by a normal conductor. The formalism takes full account of the constraints imposed by hydrostatic equilibrium with a barotropic equation of state. A characteristic of this problem is that the currents and fields need to be determined simultaneously and self-consistently. Within the core, the strong Type II limit $B \ll H$ allows us to compute the shapes of individual field lines. We specialize to purely poloidal magnetic fields that are perpendicular to the equator, and develop the "most dipolar case" in which field lines are vertical at the outer radius of the core, which leads to a magnetic field at the stellar surface that is as close to a dipole as possible. We demonstrate that although field lines from the core may only penetrate a short distance into the normal shell, boundary conditions at the inner radius of the normal shell control the field strength on the surface. Remarkably, we find that for a Newtonian $N = 1$ polytrope, the surface dipole field strength is $B_{\rm surf} \simeq H_b \epsilon_b / 3$ where H_b is the magnetic field strength at the outer boundary of the Type II core and $\epsilon_b R$ is the thickness of the normal shell. For reasonable models, $H_b \approx 10^{14}$ G and $\epsilon_b \approx 0.1$ so the surface field strength is $B_{\rm surf} \simeq 3 \times 10^{12}$ G, comparable to the field strengths of many radiopulsars. In general, H_b and ϵ_b are both determined by the equation of state of nuclear matter and by the mass of the neutron star, but $B_{\rm surf} \sim 10^{12}$ G is probably a robust result for the "most dipolar" case. We speculate on how the wide range of neutron star surface fields might arise in situations with less restrictions on the internal field configuration. We show that quadrupolar distortions are

[1]Previously published as Henriksson, K. T. and Wasserman, I.: 2013, *Mon. Not. R. Astron. Soc.* **431(4)**, 2986.

$\sim -10^{-9}(H_b/10^{14}\,\mathrm{G})^2$ and arise primarily in the normal shell for $B \ll H_b$.

2.1 Introduction

Theoretical arguments predict that the protons in the core of a neutron star form a superconductor [1], which will be Type II provided that $\kappa = 1/k_L\xi_p > 1/\sqrt{2}$, where ξ_p is the coherence length and $1/k_L$ is the London length [2]; numerically

$$\begin{aligned} k_L^2 &= \frac{4\pi n_p e^2}{m_p^\star c^2} = \frac{4p_{F,p}^3 e^2}{3\pi\hbar^3 m_p^\star c^2} = (306\,\mathrm{fm})^{-2}\left(\frac{p_{F,p}}{50\,\mathrm{MeV}}\right)^3\left(\frac{m_p}{m_p^\star}\right) \\ \xi_p &= \frac{\hbar p_{F,p}}{\pi\Delta_p m_p^\star} = \frac{3.33\,\mathrm{fm}(p_{F,p}/50\,\mathrm{MeV})}{\Delta_p(\mathrm{MeV})(m_p^\star/m_p)} \\ \kappa &= \frac{1}{k_L\xi_p} = \frac{91.8\Delta_p(\mathrm{MeV})(m_p^\star/m_p)^{3/2}}{(p_{F,p}/50\,\mathrm{MeV})^{5/2}} \end{aligned} \tag{2.1}$$

where $m_p^\star$ is the proton effective mass [e.g. 31–34]. The gap energy in MeV is $\Delta_p(\mathrm{MeV}) = 0.15T_{c,p,9}$ for a critical temperature $T_{c,p} = 10^9 T_{c,p,9}\,\mathrm{K}$ (because the pairing is ${}^1S_0$) and $n_p = p_{F,p}^3/3\pi^2\hbar^3$ is the proton density. We expect $p_{F,p} \simeq 50$ MeV at or just below nuclear density, $n_{\mathrm{nuc}} = 0.16\,\mathrm{fm}^{-3}$, which is near the boundary between the superconducting core and normal conducting crust inside a neutron star [35, 36] Although calculations of Δ_p are still being refined [3, 4], (2.1) is likely to be consistent with Type II superconductivity for $n_b \lesssim 2n_{\mathrm{nuc}}$.

Two recent observations are relevant to this question. First, X-ray observations of the Cassiopeia A neutron star are consistent with cooling via the Cooper pair formation process [5–7], and require proton superconductivity to suppress the contribution from URCA processes, particularly Modified URCA; if $T_{c,p,9} \gtrsim 2-3$ throughout the Cassiopeia A neutron star, these processes are unimportant [6]. Second, the discovery of a $2M_\odot$ neutron star favors relatively stiff equations of state of nuclear matter, in which case internal densities may not be far above n_{nuc} [8]. We can quantify using relativistic polytropes, where the relationship between pressure P and baryon density n_b is $P \propto n_b^{1+1/N}$; to fix the scale we use the chemical

potential is $\mu_{\rm nuc} = m_b(1+\epsilon_{\rm nuc})$ at nuclear density, where m_b is the baryon mass. Requiring (i) $\epsilon_{\rm nuc} = 0.065$, a reasonable value [37], (ii) $M_{\rm max} > 2M_\odot$ and (iii) sound speed < 1 implies $0.54 \le N \le 0.73$, for which $M_{\rm max} \approx 5.44(\epsilon_{\rm nuc})^{N/2} M_\odot \simeq 2.0 - 2.6 M_\odot$, and central densities are $n_b/n_{\rm nuc} \simeq 1.7-2.4$ and $n_b/n_{\rm nuc} \simeq 2.4-6.7$ for $M = 1.4M_\odot$ and $M = 2.0M_\odot$, respectively. Actual equations of state may be stiffer than $N = 1$ in some density ranges, and softer in others, but central densities may not be much larger than $\simeq 2n_{\rm nuc}$ for "typical" neutron stars. In this relatively limited density range, and with $T_{c,p,9} \gtrsim 2-3$, $\kappa > 1/\sqrt{2}$ is likely to be true, so the superconductor is Type II.

Inside a Type II superconductor, magnetic flux is concentrated within flux tubes, each of which carries magnetic flux $\Phi_0 = \pi\hbar c/e \approx 2.06 \times 10^{-7}\,{\rm G\,cm^2}$. The spacing between flux tubes in a triangular lattice is $\ell_B = (2\Phi_0/B\sqrt{3})^{1/2} = 4880 B_{12}^{-1/2}$ fm, where $B = 10^{12}B_{12}$ G is the magnitude of the magnetic induction in the core; consequently

$$k_L \ell_B = 15.9 B_{12}^{-1/2} \left(\frac{p_{F,p}}{50\,{\rm MeV}}\right)^{3/2} \left(\frac{m_p}{m_p^\star}\right)^{1/2} \quad . \tag{2.2}$$

When $k_L\ell_B \gg 1$, the magnetic field is confined to flux tubes that do not interact with one another to a first approximation; the local magnetic field near a flux tube decays exponentially with a scale length $1/k_L$. Under these circumstances, the magnetic free energy is nearly proportional to B and the magnetic field strength inside the superconductor is approximately [2]

$$H \simeq H_{c1} \simeq \frac{\Phi_0 k_L^2 \ln\kappa}{4\pi} = \frac{p_{F,p}^3 e \ln\kappa}{3\pi m_p^\star c\hbar^2} = 8.75\times 10^{13}{\rm G} \left(\frac{\ln\kappa}{5}\right) \left(\frac{p_{F,p}}{50\,{\rm MeV}}\right)^3 \left(\frac{m_p}{m_p^\star}\right) \tag{2.3}$$

which is a function of density, since $p_{F,p}$, $m_p^\star$ and κ vary with density according to the neutron star equation of state; from the calculations in [3], we conclude that a fairly good approximation is $H \propto \rho^b$ with $b \approx 1.6 - 1.8$. Since $k_L\ell_B$ is large, the superconducting core of a neutron star is in the "strong Type II" regime. That the magnetic field strength in this

regime is fixed by the density both simplifies and complicates the computation of magnetic structure. The strong Type II limit fails within a (presumably thin) transition region within which protons cluster progressively into nuclei until the superconducting free proton fluid disappears entirely. The outer shell of the neutron star is then a normal conductor.

The challenge is to compute the magnetic field structure including both Type II inner core and normal outer shell, which then matches to the (vacuum) exterior. In this paper, we focus on the "most dipolar" external fields within stars we model as $N = 1$ Newtonian polytropes. In order to find these most dipolar configurations, we require that field lines exit the core vertically. We then show that if $H_b \gg B$ is the magnetic field strength at the outer edge of the Type II core, then the magnetic field at the base of the normal shell is very nearly $-H_b \sin\theta\,\hat{\boldsymbol{\theta}}$, provided that the transition region between the core and normal shell is thin enough. This boundary condition is consistent with a particular dipole field solution within the normal shell. From this solution we find that the characteristic magnetic dipole field strength at the stellar surface under these conditions is approximately

$$\frac{\mu}{R^3} \simeq \frac{H_b \epsilon_b}{3} \simeq 2.91 \times 10^{12}\mathrm{G} \left(\frac{\ln\kappa}{5}\right) \left(\frac{p_{F,p}}{50\,\mathrm{MeV}}\right)^3 \left(\frac{m_p}{m_p^\star}\right) \left(\frac{\epsilon_b}{0.1}\right) \ . \tag{2.4}$$

where the thickness of the crust is $\epsilon_b R$ and μ is the dipole moment.

Equation (2.4) is one of the central results of this paper: it relates the dipole magnetic field strength directly to the magnetic field in the Type II core and the thickness of the stellar crust, both of which may be computed given the nuclear equation of state. Although (2.4) depends sensitively on $p_{F,p}$ at the boundary of the Type II core, it is noteworthy that the implied field strength in this model is comparable to $B \sim 10^{12}$ G, which is characteristic of many pulsars and accreting neutron stars. Detailed results will differ among equations of state; in particular, $\epsilon_b \propto \rho_b^{1/N}$, where ρ_b is the density at the base of the normal shell, for a polytrope of index N.

Other calculations based on magneto-thermal effects and evolution have also arrived at surface magnetic field strengths of order $10^{12} - 10^{13}$ G [38, 39]. These arguments did not consider the Type II core, and the significant boundary condition it imposes at the base of the neutron star's normal outer shell.

In section 2.2 we present a general overview of the problem we address here. In this section, we derive (i) the implications of hydrostatic balance for magnetic field configurations, (ii) the equations that we solve in the Type II core, (iii) the equations that hold in the normal shell, and (iv) the formalism for computing stellar distortions. We give specific results relevant to the "most dipolar" case and derive, in particular, (2.4), but also highlight causes of perturbations around this simple solution. In section 2.3 we illustrate some of the salient features of the problem via a toy model that is totally analytic and surprisingly close to being realistic. Then in section 2.4 we present particular results for the most dipolar case of greatest interest. In this section, we consider not only the simplest version of the "most dipolar" case but also perturbations around that solution that lead to non-dipolar corrections to the fields. We conclude in section 2.5 by reviewing these solutions and suggesting extensions to other cases that may allow surface field strengths that are either appreciably lower or higher than (2.4).

2.2 Overview

In this paper, we compute the magnetic field for a star with a superconducting core that matches onto a normal crust surrounded by vacuum. We model the star as a Newtonian $N = 1$ polytrope with a poloidal magnetic field that only distorts the star slightly. Previous calculations of this type were done for poloidal fields of a uniform density star [10] and for toroidal magnetic fields in a Newtonian $N = 1$ polytrope [11–13]. These two different previous calculations were simpler than those presented here. A significant complication in finding the magnetic field structure is that H is density-dependent according to (2.3);

accommodating this complication will require a generalization of the method of solution for a uniform density star [10]. Calculations for a toroidal field could account for the density dependence of H because it was unnecessary to determine the field line shapes, which were specified *a priori* [11].

Our calculations are perturbative in that we assume that the distortions induced by magnetic stresses (which we compute) are small. However, we take full account of the requirements of hydrostatic balance, which constrain the field shapes, just as for normal conductors [40, 41]; our calculations are analogous to those done previously for small magnetic distortions in a normal conductor [9]. We find the "true equilibrium" configurations in which the magnetic distortions are assumed to obey the same equation of state as the unperturbed star. The actual magnetic fields in neutron stars may not be true equilibria in this sense [42] even though, on sufficiently long time scales, the fields should relax to these states naturally. Even in non-equilibrium field configurations the field at the base of the normal shell will have to match properly to the field in the Type II core. We therefore expect a version of (2.4) to remain true for substantially dipolar fields even for configurations that are not true equilibria.

We focus on the "most dipolar" field configurations that arise when field lines hit the outer edge of the Type II core vertically. As we shall see, this is a special configuration, and infinitely many others are possible.

Throughout this paper, we assume that the entire core of the star is superconducting. We argued above that this may be reasonable if the density range in the core is not too large. We expect that the external dipole field that emerges from our "most dipolar" solutions would not be affected significantly if the very inner core of the neutron star is not superconducting.

2.2.1 Requirements of Hydrostatic Balance

The magnetic free energy is $f(\rho, \mathbf{B})$, where ρ is mass density and $\mathbf{B}$ is magnetic induction; then the magnetic field is $\boldsymbol{H} = 4\pi\partial f/\partial\mathbf{B}$, and the magnetic force density is

$$\mathbf{f}^{\rm mag} = -\rho\boldsymbol{\nabla}\left(\frac{\partial f}{\partial\rho}\right) + \frac{(\boldsymbol{\nabla}\times\mathbf{H})\times\mathbf{B}}{4\pi} = -\rho\boldsymbol{\nabla}\left(\frac{\partial f}{\partial\rho}\right) + \frac{\mathbf{J}\times\mathbf{B}}{c} \tag{2.5}$$

using Ampére's law, $\boldsymbol{\nabla}\times\mathbf{H} = 4\pi\mathbf{J}/c$. Equation (2.5) was derived in [11] by taking the divergence of the magnetic stress tensor for a Type II superconductor given by [2]; it may also be derived by considering the variation of magnetic energy resulting from small fluid displacements. The equation of hydrostatic balance including pressure, gravity and magnetic forces is

$$0 = -\frac{\boldsymbol{\nabla}P}{\rho} - \boldsymbol{\nabla}\Psi + \frac{\mathbf{f}^{\rm mag}}{\rho} \tag{2.6}$$

where Ψ is the gravitational potential, P is the pressure and ρ is the mass density. For a barotropic fluid $P = P(\rho)$ and $dh(\rho) = dP(\rho)/\rho$, in which case

$$0 = -\boldsymbol{\nabla}\left(h + \Psi + \frac{\partial f}{\partial\rho}\right) + \frac{\mathbf{J}\times\mathbf{B}}{\rho c} \ . \tag{2.7}$$

Equation (2.7) is only consistent mathematically if $\mathbf{J}\times\mathbf{B}/\rho c = -\boldsymbol{\nabla}\Phi$, where Φ is some potential. In axisymmetry,

$$\mathbf{B} = \boldsymbol{\nabla}\times\left[\frac{A(r,\theta)\,\hat{\boldsymbol{\phi}}}{r\sin\theta}\right] + B_T(r,\theta)\,\hat{\boldsymbol{\phi}} \tag{2.8}$$

and $\mathbf{H} = \mathbf{H}_P + H_T\,\hat{\boldsymbol{\phi}}$; the current density is

$$\boldsymbol{\nabla}\times\mathbf{H} = \boldsymbol{\nabla}\times\mathbf{H}_P + \frac{\boldsymbol{\nabla}(H_T r\sin\theta)\times\hat{\boldsymbol{\phi}}}{r\sin\theta} \equiv \frac{4\pi J\,\hat{\boldsymbol{\phi}}}{c} + \frac{\boldsymbol{\nabla}(H_T r\sin\theta)\times\hat{\boldsymbol{\phi}}}{r\sin\theta} \ . \tag{2.9}$$

Requiring that $\hat{\boldsymbol{\phi}}\cdot(\mathbf{J}\times\mathbf{B}) = 0$ implies that $H_T r\sin\theta = \mathcal{H}_T(A)$; the Lorentz acceleration $\mathbf{J}\times\mathbf{B}/\rho c$ is a total gradient if

$$J - \frac{cB_T}{4\pi}\frac{d\mathcal{H}_T(A)}{dA} = c\rho r\sin\theta\mathcal{J}(A) \tag{2.10}$$

which means that $-\boldsymbol{\nabla}\Phi = \mathcal{J}(A)\boldsymbol{\nabla}A$. Equation (2.10) is well-known for normal magnetic equilibria [9, 40, 41, 43]; the $B_T = 0$ version of (2.10) has also been derived previously for Type II superconductors with poloidal fields [10, 12]. Similar results have been derived independently by Lander [44].

We are interested in poloidal fields only, so $B_T = 0$. [See also 44, for specific models including poloidal and toroidal fields.] We also assume that $f(\rho, \mathbf{B}) = f(\rho, B)$ i.e. there are no preferred directions in space so the free energy only depends on $B = |\mathbf{B}|$. In this situation, the magnetic field and magnetic induction are parallel: $\boldsymbol{H} = 4\pi\hat{\boldsymbol{B}}\partial f/\partial B$ where $\hat{\boldsymbol{B}} = \mathbf{B}/B$.

Our goal is to solve

$$\boldsymbol{\nabla}\times\boldsymbol{H} = \boldsymbol{\nabla}\times(H\hat{\boldsymbol{B}}) = \boldsymbol{\nabla}H\times\hat{\boldsymbol{B}} + H\boldsymbol{\nabla}\times\hat{\boldsymbol{B}} = 4\pi\rho r\sin\theta\mathcal{J}(A)\,\hat{\boldsymbol{\phi}} \tag{2.11}$$

throughout the star. We shall strive for solutions without surface currents; in particular, we are interested in solutions in which field lines cross the equator smoothly and vertically. With this goal in mind, we will have to determine *both* the field configuration *and* its source $\mathcal{J}(A)$ self consistently, within both the Type II core and the normal shell.

2.2.2 Field Configuration in the Type II Core

In the strong Type II limit, $H = H(\rho)$ in the core, and invoking the assumption that magnetic distortions are small, we can substitute the unperturbed density of the background star, $\rho(r)$, so $H = H(r)$.

With this simplification, (2.11) is a complicated partial differential equation even if we specify $\mathcal{J}(A)$ somehow, and we shall not attempt to solve it directly. Instead, we extend the procedure first employed by Roberts [10] for uniform density stars to stars with $H(r) \neq$ constant. Since $B_T = 0$, (2.8) implies that $\hat{\boldsymbol{B}}\cdot\boldsymbol{\nabla}A = 0$ i.e. A is constant along poloidal field lines. This allows us to consider (2.11) along individual field lines.

Let us concentrate on a particular field line. Introduce the parametric independent variable s, the arc length along this field line; position along the field line is $\mathbf{r}(s)$ and the tangent to the field line is $\hat{\boldsymbol{B}}(s) = d\mathbf{r}(s)/ds$. There are two directions normal to the field line: $\hat{\boldsymbol{\phi}}$ and a second direction $\hat{\boldsymbol{n}}(s)$ which we define to be $\hat{\boldsymbol{n}}(s) = \hat{\boldsymbol{\phi}}\times\hat{\boldsymbol{B}}(s)$. The field line curvature is $K(s)$ given by $K(s)\hat{\boldsymbol{n}}(s) = d^2\mathbf{r}(s)/ds^2 = \hat{\boldsymbol{B}}(s)\cdot\boldsymbol{\nabla}\hat{\boldsymbol{B}}(s)$. Equation (2.11) is then equivalent to

$$\frac{4\pi J}{c} = 4\pi\rho r\sin\theta\mathcal{J}(A) = -\boldsymbol{\nabla}H\cdot\hat{\boldsymbol{n}} + KH \ . \tag{2.12}$$

For uniform H the first term in (2.12) is absent and we recover the equation found by Roberts [10]. In (2.12) $\mathcal{J}(A)$ is simply a constant associated with the field line.

In axisymmetry, we may choose to specify position along a field line by $r(s)$ and $\theta(s)$; in that case

$$\hat{\boldsymbol{B}}(s) = \frac{dr(s)}{ds}\,\hat{\boldsymbol{r}} + r(s)\frac{d\theta(s)}{ds}\,\hat{\boldsymbol{\theta}} \equiv \cos\Lambda(s)\,\hat{\boldsymbol{r}} + \sin\Lambda(s)\,\hat{\boldsymbol{\theta}} \tag{2.13}$$

and therefore

$$\hat{\boldsymbol{n}}(s) = \hat{\boldsymbol{\phi}}\times\hat{\boldsymbol{B}}(s) = -\sin\Lambda(s)\,\hat{\boldsymbol{r}} + \cos\Lambda(s)\,\hat{\boldsymbol{\theta}} \ . \tag{2.14}$$

The field line curvature is

$$K(s) = \frac{d\Lambda}{ds} + \frac{\sin\Lambda}{r} \ ; \tag{2.15}$$

using (2.14) and (2.15) in (2.12) we find

$$\frac{d\Lambda}{ds} = \frac{4\pi\rho r\sin\theta\mathcal{J}(A)}{H(r)} - \frac{\sin\Lambda}{r}\left(\frac{r}{H}\frac{dH(r)}{dr} + 1\right) \ . \tag{2.16}$$

Equations (2.16) and (2.13) determine the field line shape jointly, given $\rho(r)$, $H(\rho)$ and a value of $\mathcal{J}(A)$.

For our solutions we shall assume an $N = 1$ polytrope for which $\rho(r) = \rho(0) \sin x/x$, with $x = \pi r/R$; we shall also assume $H \propto \rho^b$. With these choices, and the definition $ds = Rd\sigma/\pi$, (2.16) becomes

$$\frac{d\Lambda}{d\sigma} = \frac{\hat{\mathcal{J}}(A) x^b \sin\theta}{(\sin x)^b} - \frac{\sin\Lambda}{x}\left[b(x\cot x - 1) + 1\right] \tag{2.17}$$

where

$$\hat{\mathcal{J}}(A) = \frac{4R^2\rho(0)\mathcal{J}(A)}{\pi H(0)} \ ; \tag{2.18}$$

the field line shape is found by solving (2.17) along with

$$\frac{dx}{d\sigma} = \cos\Lambda \qquad x\frac{d\theta}{d\sigma} = \sin\Lambda \ . \tag{2.19}$$

We are interested in solutions that start at some equatorial footpoint where $x = x(0)$ and $\theta(0) = \pi/2$. At this footpoint, symmetry dictates that the field line be perpendicular to the equator; choosing the direction to be vertically upward implies $\Lambda(0) = -\pi/2$.

For the "most dipolar" case we also want field lines to hit the outer boundary of the Type II region at $x = x_b$ with $\Lambda = -\theta$. Very generally, it is impossible to find solutions that are exactly vertical throughout the core for a given $H(\rho)$. (The solutions are nevertheless close to the toy model developed in section 2.3 that demands that field lines *are* exactly vertical.) The condition that a field line starts out at $x(0)$ and $\theta = \pi/2$ pointing vertically and also hits vertically at x_b determines the value of $\hat{\mathcal{J}}(A)$ for that field line. Note that in this context, "A" is just a label for the field line; we could just as well label the field line by $x(0)$. In fact, this procedure *does not* determine $A(x, \theta)$ within the Type II core. The end result is $\hat{\mathcal{J}}(x(0))$ and, since field lines hit x_b at $\theta(x(0))$, $\hat{\mathcal{J}}_b(\theta)$ is determined parametrically on the outer boundary of the core.

We can also consider other types of solution for field lines, for instance solutions in which field lines hit x_b with some other specified set of orientations and, therefore, carry different values of $\hat{\mathcal{J}}(x(0))$ along with them. We must be careful to choose orientations for which field lines do not cross within the Type II core. But even that restriction allows many different possibilities other than our "most dipolar" case.

As an illustration, figure 2.1 shows the field lines assuming that field lines intersect the outer boundary of the core *radially*. For $H_b \gg B$, this is the field configuration needed to match smoothly into regions without currents since $|B_\theta| \sim |B_r|$ in that case [e.g. 10]. The current free region may be the normal shell or the vacuum exterior. In order to highlight the effects of variable H and ρ inside the core, we show three different cases: (a) $H \propto \rho^{1.6}$ with a $N = 1$ polytrope density profile; (b) H and ρ uniform, the case considered by Roberts [10]; (c) H uniform but with a $N = 1$ polytrope density profile. The lower right panel of figure 2.1 shows $\hat{\mathcal{J}}_b$ on the boundary of the Type II core, which we placed at $r_b = 0.9R$, as a function of $\sin^2\theta$. As can be seen from figure 2.1 the current diverges for field lines near the equator. This is because they start out vertical and must turn through about $\pi/2$ to hit the boundary radially within the short distance $r_b - r$.

The fact that we do not determine $A(x, \theta)$ in the Type II core means that even with a given set of solutions for individual field lines, we can consider various "field line densities" within the core. This freedom can accommodate theories of field line evolution in which secular motion of flux tubes leads to different concentrations of flux within the core.

2.2.3 Solution in the Normal Shell

Within the normal shell, it is most straightforward to solve (2.11) directly: using $\boldsymbol{H} = \boldsymbol{B}$ and substituting for the poloidal field we get

$$-\frac{H(0)R^2}{\pi^2}[\hat{\mathcal{J}}(A)x\sin x\sin^2\theta] = \frac{\partial^2 A}{\partial x^2} + \frac{1}{x^2}\left(\frac{\partial^2 A}{\partial \theta^2} - \cot\theta\frac{\partial A}{\partial \theta}\right) \ , \tag{2.20}$$

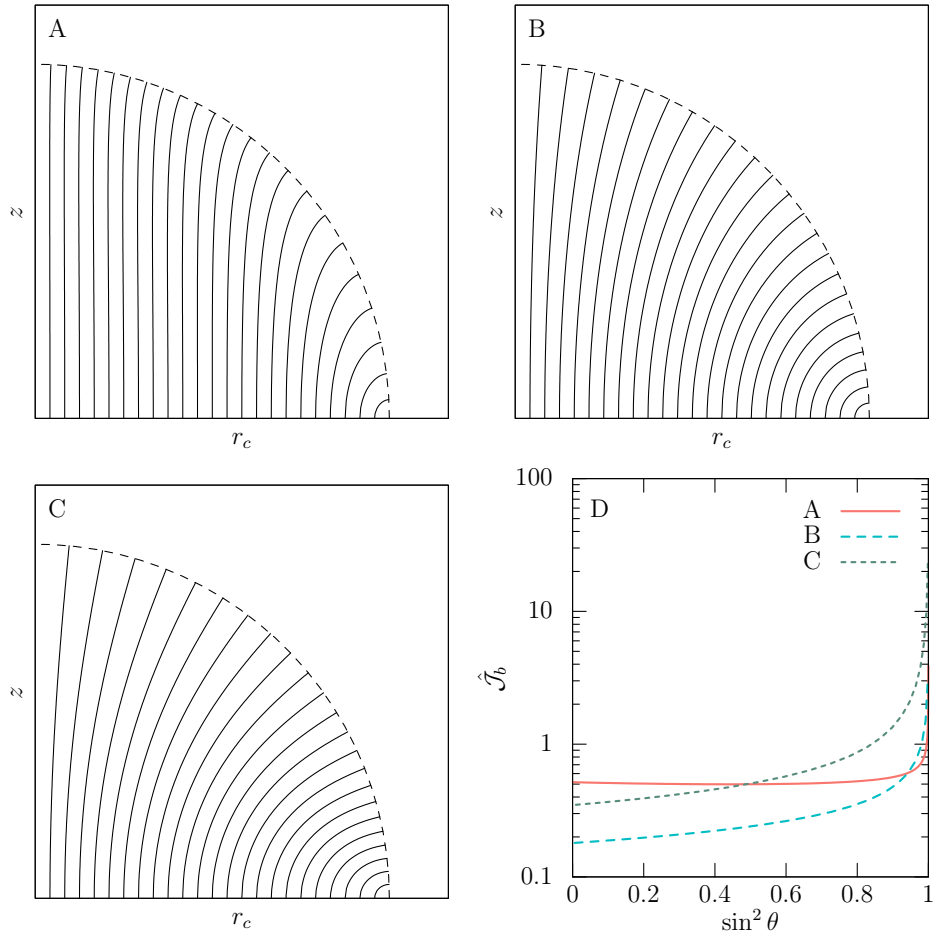

Figure 2.1: Field line configurations in the Type II core for field lines that hit the core boundary radially. Panel A shows field lines for $H \propto \rho^{1.6}$ and a $N = 1$ polytrope density profile; panel B shows field lines for uniform H and ρ; panel C shows field lines for uniform H but a $N = 1$ polytrope density profile. All three models assume that the core radius is $r_b = 0.9R$, shown on the plots as a dashed line. Panel D shows the rescaled current parameter $\hat{\mathcal{J}}$ for the three models as a function of $\sin^2\theta$ on r_b.

where we have used the same parametrization as in (2.18) and specialized to the $N = 1$ polytrope density profile. Equation (2.20) would be straightforward to solve *given* $\hat{\mathcal{J}}(A)$. However, we have to determine $\hat{\mathcal{J}}(A)$ to be consistent with matching conditions at both the inner boundary of the normal shell at x_b and at the stellar surface, where the field must match smoothly to vacuum.

Matching to a vacuum exterior is accomplished most easily by introducing the expansion

$$A(x,\theta) = \sin\theta \sum_{j=0}^{\infty} A_j(x) {P_{2j+1}}^1(\cos\theta) \tag{2.21}$$

where ${P_{2j+1}}^1(\mu)$ is an associated Legendre polynomial. Using (2.21) in (2.20) implies

$$\frac{d^2A_j(x)}{dx^2} - \frac{(2j+2)(2j+1)A_j(x)}{x^2} = -\frac{H(0)R^2 x\sin x}{\pi^2 N_j}\int_{-1}^{+1} d\mu\sqrt{1-\mu^2}{P_{2j+1}}^1(\mu)\hat{\mathcal{J}}(A) \tag{2.22}$$

where

$$N_j = \frac{2(2j+2)(2j+1)}{4j+3}\ . \tag{2.23}$$

The source term in (2.22) generally involves the entire set of A_i, not just $i = j$. But once $\hat{\mathcal{J}}(A)$ has been determined, the source term is known, and the boundary condition at the surface $x = \pi$ is

$$\left(\frac{dA_j(x)}{dx}\right)_\pi + \frac{(2j+1)A_j(\pi)}{\pi} = 0 \tag{2.24}$$

for matching to a vacuum field in the exterior.

Matching to the core requires that the normal component of $\mathbf{B}$ and tangential component of $\mathbf{H}$ be continuous across the boundary. In the simplest case, the transition zone thickness may be neglected. If $\Lambda_b(\theta)$ is the value of Λ for a field line hitting x_b at θ and $B(\theta)$ is the

magnitude of the core induction field there, then the matching conditions are ($\mu = \cos\theta$)

$$\begin{aligned} \left(\frac{\partial A}{\partial \mu}\right)_b &= -\frac{R^2 x_b^2 B(\theta)\cos\Lambda_b(\theta)}{\pi^2} \\ \left(\frac{\partial A}{\partial x}\right)_b &= -\frac{R^2 x_b H_b \sin\theta \sin\Lambda_b(\theta)}{\pi^2} \ . \end{aligned} \tag{2.25}$$

In the strong Type II regime, $B(\theta) \ll H_b$ and unless $\Lambda_b(\theta) \lesssim B/H_b$ the field is predominantly tangential at the base of the normal shell. To a first approximation, $(\partial A/\partial\mu)_b \approx 0$, which is equivalent to $A_j(x_b) \approx 0$, in the strong Type II regime.

Equations (2.24) and (2.25) impose three conditions on each $A_j(x)$, which is one too many. This overdetermination implies constraints on the form of $\hat{\mathcal{J}}(A)$ within the shell.

In the "most dipolar" case, $\Lambda_b(\theta) = -\theta$, and (2.25) implies that the field at the inner edge of the normal shell is approximately $-H_b \sin\theta\, \hat{\boldsymbol{\theta}}$ in the limit $B \to 0$. In this limit, field lines from the interior do not penetrate into the normal shell but still influence conditions there via (2.25). With $B = 0$, the field inside the normal shell is precisely dipolar, $A(x,\theta) = A_0(x)\sin^2\theta$, where

$$\begin{aligned} A_0(x) &= \frac{H_b R^2 f(x;x_b)}{3\pi^2} \\ f(x;x_b) &= \frac{x^3 - x_b^3 + 6x\cos x - 6x_b\cos x_b + (3x^2-6)\sin x - (3x_b^2-6)\sin x_b}{x(1+\cos x_b)} \ . \end{aligned} \tag{2.26}$$

Within the shell, consistency with (2.24) and (2.25) requires that

$$\hat{\mathcal{J}}(A) = \hat{\mathcal{J}}_{\rm shell} = \frac{H_b}{H(0)(1+\cos x_b)} = \frac{(\sin x_b/x_b)^b}{1+\cos x_b} \tag{2.27}$$

which is the simplest case showing how the boundary conditions determine $\hat{\mathcal{J}}(A)$. The stellar dipole moment is

$$\mu = RA_0(\pi) = \frac{H_b R^3 f(\pi;x_b)}{3\pi^2} \ ; \tag{2.28}$$

if $\pi - x_b \equiv \delta_b = \pi\epsilon_b \ll 1$, $f(\pi; x_b)/3\pi^2 \approx \delta_b/3\pi = \epsilon_b/3$, which leads to (2.4) for thin shells.

Equation (2.26) holds when we can neglect the thickness of the transition layer and the radial field that pokes into the normal shell through it. If the transition layer is thin enough, then its effect is to introduce a "surface current" into the jump condition from the Type II core to the normal shell: the tangential field at the base of the normal shell is now

$$B_\theta(x_b, \theta) = -\frac{\pi^2}{R^2 x_b \sin\theta}\left(\frac{\partial A}{\partial x}\right)_b = H_b \sin\Lambda_b(\theta) + \frac{\pi\ell\hat{\mathcal{J}}_b(\theta)H(0)\sin x_b \sin\theta}{R} \tag{2.29}$$

where ℓ is the thickness of the transition zone. Section 2.B contains a brief discussion of the rather complex physics of this region. There, it is shown that (2.29) holds as long as field lines do not rotate very much as they pass through the transition zone. Roughly speaking, this will be true provided that $H_b\ell/BR \ll 1$; therefore the second term in (2.29) is $\ll BH(0)/H_b^2$ times the first. Nevertheless, (2.29) perturbs the solution away from (2.26) even in the "most dipolar" case. In particular, the jump term engenders non-dipolar fields in the shell and outside, and requires a more detailed calculation of $\hat{\mathcal{J}}(A)$ inside the shell. As long as the corrections to (2.26) are small they may be computed perturbatively. A method of calculation is outlined in appendix 2.A.

Relaxing the $B \to 0$ limit also perturbs the solution even if the transition zone thickness is negligible. If we assume that

$$A(x_b, \theta) = \frac{1}{2}Br_b^2\sin^2\theta = \frac{BR^2x_b^2\sin^2\theta}{2\pi^2} \tag{2.30}$$

then the unperturbed field inside the normal shell remains dipolar, and is altered to $A_0(x, \theta) = A_0(x; B)\sin^2\theta$, where

$$A_0(x; B) = \frac{BR^2x_b^3}{2\pi^2 x} + \frac{(H_b + B/2)R^2 f(x; x_b)}{3\pi^2} \tag{2.31}$$

and the current density parameter is

$$\hat{\mathcal{J}}_{\rm shell} = \frac{H_b(1 + B/2H_b)}{H(0)(1 + \cos x_b)} \ . \tag{2.32}$$

Equation (2.31) implies a magnetic moment

$$\mu(B) = \frac{Br_b^3}{2} + \frac{(H_b + B/2)R^3 f(\pi; x_b)}{3\pi^2} \tag{2.33}$$

which reduces to (2.28) for $B = 0$; the first term in (2.33) is simply the dipole moment associated with B and the second arises from the currents in the normal shell. Figure 2.2 shows A_0/r^2 and $-r^{-1}dA_0/dr$ in the normal shell, where the magnetic field is $\boldsymbol{H} = \boldsymbol{B} = (2A_0/r^2)\cos\theta\,\hat{\boldsymbol{r}} - (r^{-1}dA_0/dr)\sin\theta\,\hat{\boldsymbol{\theta}}$. In the limit that the transition from superconductor to normal conductor takes place within a region of zero thickness, H is discontinuous at the boundary between core and shell, but the radial component of $\boldsymbol{B}$ and the $\hat{\boldsymbol{\theta}}$ component of $\boldsymbol{H}$ are continuous, as required by Maxwell's equations with no surface currents. Appendix 2.B outlines how $\boldsymbol{H}$ field changes smoothly when the transition region has nonzero thickness. Within the Type II core, $H = H(\rho)$ is independent of θ.

Equation (2.31) implies that magnetic field lines from the core enter the shell. The bounding field line entering from the core has $A = \frac{1}{2}Br_b^2$, and therefore defines a region $\theta \le \theta_{\rm II}(x)$ where

$$\sin^2\theta_{\rm II}(x) = \frac{\beta}{\beta x_b/x + \tilde{f}(x; x_b)} \ ; \tag{2.34}$$

in (2.34)

$$\beta \equiv \frac{3\pi^2 Br_b^2}{(2H_b + B)R^2 f(\pi; x_b)} \qquad \tilde{f}(x; x_b) \equiv \frac{f(x; x_b)}{f(\pi; x_b)} \ . \tag{2.35}$$

The region occupied by the field lines is small if $\beta \sim B/H_b\epsilon_b \ll 1$; note that this is more restrictive than the condition for validity of the strong Type II regime, $B \ll H_b$. Equation (2.34) indicates that the bounding field line rises from $\theta = \pi/2$ close to x_b, remaining at

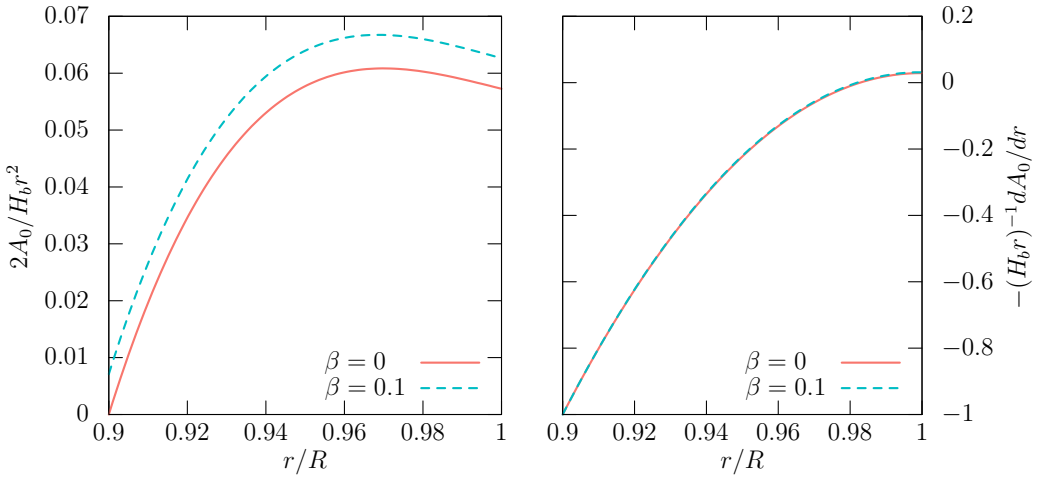

Figure 2.2: $2A_0/H_b r^2$ (left panel) and $-(H_b r)^{-1} dA_0/dr$ (right panel) in the normal shell, where $\boldsymbol{H} = \boldsymbol{B} = (2A_0/r^2)\cos\theta\,\hat{\boldsymbol{r}} - (r^{-1}dA_0/dr)\sin\theta\,\hat{\boldsymbol{\theta}}$. For the functional form of A_0, see (2.31). Two different values of B are assumed, parameterized by the quantity β defined in (2.35); results are shown for $\beta = 0$ and 0.1.

$\theta \sim 1$ as long as $\tilde{f}(x; x_b) \sim \beta$, which is the case for $x/x_b - 1 \lesssim \beta$. Ultimately, the bounding field lines emerge at $x = \pi$ confined to a polar cap with $\theta \lesssim \sqrt{\beta}$. The volume of the region occupied by impinging field lines is only $\sim \beta$ times the volume of the shell. In the limit $\beta \to 0$ field lines from the core *do not* penetrate into the normal shell.

However, within that volume, $\Delta\hat{\mathcal{J}}(A) = \hat{\mathcal{J}}(A) - \hat{\mathcal{J}}_{\rm shell} \neq 0$ because field lines entering from the core carry their $\hat{\mathcal{J}}(A)$ along with them. The zeroth order solution represented by (2.31) and (2.32) requires perturbative corrections driven by the difference $\Delta\hat{\mathcal{J}}(A)$ within this region; the corrections are $\mathcal{O}(\beta\Delta\hat{\mathcal{J}}(A)/\hat{\mathcal{J}}_{\rm shell})$. Appendix 2.A outlines how these corrections may be taken into account.

2.2.4 Magnetic Distortions Due to Poloidal Fields

For poloidal fields, the Lorentz acceleration is $-\boldsymbol{\nabla}\Phi = \mathcal{J}(A)\boldsymbol{\nabla}A$, so

$$\Phi(A) = -\frac{\pi H(0)}{4R^2\rho(0)} \int_0^A dA' \hat{\mathcal{J}}(A') \ , \tag{2.36}$$

and the Bernoulli equation is

$$C = h + \Psi + \frac{\partial f}{\partial \rho} + \Phi \tag{2.37}$$

where C is the Bernoulli constant. For perturbations of a $N = 1$ polytrope, if we expand in Legendre polynomials

$$\Psi(x, \theta) = \sum_l \Psi_l(x) P_l(\cos\theta) \tag{2.38}$$

we get

$$\frac{1}{x^2}\frac{d}{dx}\left[x^2 \frac{d\Psi_l(x)}{dx}\right] + \left[1 - \frac{l(l+1)}{x^2}\right]\Psi_l(x) = \delta C \delta_{l,0} - \left(\frac{\partial f}{\partial \rho} + \Phi\right)_l \equiv \delta C \delta_{l,0} + M_l(x) \tag{2.39}$$

where the magnetic potentials are expanded in the same fashion as (2.38) and δC is the perturbation of the Bernoulli constant away from its background value. The general solution of (2.39) that is regular at $x = 0$ is

$$\Psi_l(x) = \delta C \delta_{l,0} + j_l(x)\left[K_l + \int_x^\pi dx' (x')^2 y_l(x') M_l(x')\right] + y_l(x)\int_0^x dx' (x')^2 j_l(x') M_l(x') \tag{2.40}$$

where $j_l(x)$ and $y_l(x)$ are spherical Bessel functions. The constants K_0 and δC are determined by the conditions $\Psi_0(\pi) = 0 = [d\Psi(x)/dx]_\pi$, which imply

$$\delta C = K_0 = -\frac{1}{\pi}\int_0^\pi dx x^2 j_0(x) M_0(x) \ , \tag{2.41}$$

and the constants K_l are determined by the conditions $[d\Psi_l(x)/dx]_\pi + (l+1)\Psi_l(\pi)/\pi = 0$, which imply ($f_l'(x) \equiv df_l(x)/dx$)

$$0 = K_l\left[j_l'(\pi) + \frac{(l+1)j_l(\pi)}{\pi}\right] + \left[y_l'(\pi) + \frac{(l+1)y_l(\pi)}{\pi}\right]\int_0^\pi dx x^2 j_l(x) M_l(x) \ . \tag{2.42}$$

For $l > 0$,

$$\Psi_l(\pi) = -\frac{1}{\pi^2 j_l'(\pi) + (l+1)\pi j_l(\pi)} \int_0^\pi dx x^2 j_l(x) M_l(x) \ . \tag{2.43}$$

We may define the stellar multipole moment by $\Psi_l(\pi) = -GM\mathcal{M}_l/R$. With this definition, the contribution to the moment of inertia tensor resulting from the quadrupolar distortion $\mathcal{M}_2$ is $\delta\mathbf{I}_2 = -\frac{1}{3}MR^2\mathcal{M}_2(-\hat{\mathbf{x}}\,\hat{\mathbf{x}} - \hat{\mathbf{y}}\,\hat{\mathbf{y}} + 2\,\hat{\mathbf{z}}\,\hat{\mathbf{z}})$.

In the "most dipolar" case with negligible transition layer thickness and core magnetic induction, the distortion arises entirely from magnetic stresses inside the crust and is quadrupolar. In this case, ($\Theta(z) = 1$ for $z > 0$, zero otherwise)

$$M_2(x) = -\frac{H_b^2 f(x; x_b)\Theta(x - x_b)}{18\pi\rho(0)(1 + \cos x_b)} = -\frac{2H_b^2 R^3 f(x; x_b)\Theta(x - x_b)}{9\pi^2 M(1 + \cos x_b)} \tag{2.44}$$

and ($\pi^2 j_2'(\pi) + 3\pi j_2(\pi) = \pi$)

$$\mathcal{M}_2 = -\frac{2H_b^2 R^4}{9\pi^3 GM^2} \int_{x_b}^\pi \frac{dx x^2 j_2(x) f(x; x_b)}{1 + \cos x_b} \equiv -\frac{2H_b^2 R^4 \mathcal{I}(x_b)}{9\pi^3 GM^2} \ . \tag{2.45}$$

For thin shells, $\mathcal{I}(x_b) \approx 9\pi/2 = 14.14$, independent of the shell thickness; for $\epsilon_b = 0.1$, it is $\mathcal{I}(0.9\pi) = 11.44$; consequently

$$\mathcal{M}_2 = -1.39 \times 10^{-9} H_{b,14}^2 R_{10}^4 M_{1.4}^{-2} \left[\frac{\mathcal{I}(x_b)}{10}\right] \tag{2.46}$$

where $H_b = 10^{14} H_{b,14}$ G, $R = 10R_{10}$ km and $M = 1.4M_{1.4}M_\odot$. Thus, the scale of the quadrupolar distortion is determined by the value of H_b for $B/H_b \ll 1$; for terms $\mathcal{O}(B)$, see (2.54) and (2.55).

2.3 Toy Model: Vertical Field in the Core

We shall be interested in solutions that lead to external fields as close to dipolar as possible; such solutions have fields that are vertical at the outer boundary of the Type II core. In general, these will not allow field lines that are exactly vertical throughout the core.

Nevertheless, to develop a toy model, suppose $\boldsymbol{H} = H(r)\hat{\mathbf{z}}$; this model will illustrate many features of the problem. For vertical fields, $\mathcal{J}_{\rm II}(A) = \text{constant} = \mathcal{J}_{\rm II}$ and from Ampére's law

$$H(r) = \frac{4R^2\rho(0)\mathcal{J}_{\rm II}(1+\cos x)}{\pi} = \frac{1}{2}H(0)(1+\cos x) \tag{2.47}$$

where $x = \pi r/R$ and $H(R) = 0$. The dimensionless combination

$$\hat{\mathcal{J}}_{\rm II} \equiv \frac{4R^2\rho(0)\mathcal{J}_{\rm II}}{\pi H(0)} = \frac{1}{2}\ ; \tag{2.48}$$

moreover

$$b = \frac{d\ln H}{d\ln\rho} = \frac{x\sin x}{(1+\cos x)(1-x\cot x)} \tag{2.49}$$

varies monotonically between $b = 3/2$ and $b = 2$ from the center of the star to the surface. Although this model is not truly physical because $H(\rho) = H(\rho/\rho(0))$ depends on the central density, hence mass, of the star and so involves a density scale that is not the same for all stars, $3/2 \le b \le 2$ is an acceptable range for nuclear equations of state. Moreover, when we consider models with $H \propto \rho^b$ with realistic values of b, we shall see that even though $\hat{\mathcal{J}}(A)$ is no longer constant, its values are close to 0.5 for cases where field lines hit the outer boundary of the core vertically; because field lines are vertical at the equator, they remain close to vertical throughout the core in these cases, as may be seen from figure 2.3.

The interior field must match onto the field in the normal shell. If the transition from superconductor to normal conductor occurs in a transition region of negligible thickness,

then the field is dipolar in the shell to a good approximation, and is given by (2.31) and (2.32). Equation (2.32) holds generally for the dipole field within the normal shell; for the toy model $H_b = \frac{1}{2}H(0)(1+\cos x_b)$ so

$$\hat{\mathcal{J}}_{\rm shell} = \frac{1}{2}\left(1+\frac{B}{2H_b}\right) = \hat{\mathcal{J}}_{\rm II}\left(1+\frac{B}{2H_b}\right) \ . \tag{2.50}$$

The core and shell current density parameters are nearly the same in this toy model for $B/2H_b \ll 1$. This will also be true for more realistic models, but the difference will be ~ 0.1, not $\sim B/H_b$. For the toy model, the perturbations caused by $\Delta\hat{\mathcal{J}}(A)$ are very small, since $\beta(\hat{\mathcal{J}}_{\rm II} - \hat{\mathcal{J}}_{\rm shell}) = \frac{1}{2}\beta B\hat{\mathcal{J}}_{\rm II}/H_b$, and we shall ignore them; for realistic models, where $\hat{\mathcal{J}}_{\rm II} - \hat{\mathcal{J}}_{\rm shell} \sim 0.1$, the perturbations are larger, $\sim 0.1\beta$.

In general, there will be a contribution to the stellar distortion $\propto B$. One reason is that $H_b \to H_b + B/2$ in the dipole solution within the shell; thus we substitute $H_b^2 \to (H_b + B/2)^2 \simeq H_b^2 + H_b B$ in (2.45). There are also contributions from the terms in the solution that are $\propto B$. For the toy model with $\hat{\mathcal{J}}_{\rm II} = \frac{1}{2} \simeq \hat{\mathcal{J}}_{\rm shell}$ the extra $l=2$ contribution to the driving term is

$$\Delta M_2(x) = -\frac{\pi H(0) B r_b^2}{24 R^2 \rho(0)} \begin{cases} (x/x_b)^2 & \text{if } x \le x_b \\ x_b/x & \text{if } x_b \le x \le \pi \end{cases} \tag{2.51}$$

which implies an additional quadrupole moment

$$\Delta\mathcal{M}_2 = -\frac{H(0) B r_b^2 R^2 \Delta\mathcal{I}(x_b)}{6\pi G M^2} = -\frac{1.03\times 10^{-9} H_{b,14}^2 R_{10}^4 \Delta\mathcal{I}(x_b)}{M_{1.4}^2}\,\frac{B}{H_b} \tag{2.52}$$

where $\Delta\mathcal{I}(x_b) = \Delta\mathcal{I}_{\rm II}(x_b) + \Delta\mathcal{I}_{\rm shell}(x_b)$ with core and shell contributions

$$\begin{aligned}\Delta\mathcal{I}_{\rm II}(x_b) &= \frac{2(r_b/R)^2}{1+\cos x_b}\left[\left(\frac{15}{x_b^2}-6\right)\sin x_b + \left(x_b - \frac{15}{x_b}\right)\cos x_b\right] \\ \Delta\mathcal{I}_{\rm shell}(x_b) &= \frac{2(r_b/R)^2}{1+\cos x_b}\left[-x_b(1+\cos x_b) + 3\sin x_b\right] \end{aligned} \tag{2.53}$$

respectively. The crust contribution $\Delta\mathcal{I}_{\rm shell}(x_b)$ is the same in realistic models. For thin shells, $\Delta\mathcal{I}_{\rm shell}(x_b) \simeq 12/\delta_b$ and $\Delta\mathcal{I}_{\rm shell}(0.9\pi) = 26.1$. The core contribution $\Delta\mathcal{I}_{\rm II}(x_b)$ will be close to the value in the toy model, with differences arising because field lines are not strictly vertical, realistically. For thin shells, $\Delta\mathcal{I}_{\rm II}(x_b) \simeq (60/\pi - 4\pi)/\delta_b^2 \simeq 6.5/\delta_b^2$ in the toy model and $\Delta\mathcal{I}_{\rm II}(0.9\pi) = 35.8$. Comparing (2.52) with (2.46) we see that $|\Delta\mathcal{M}_2| \lesssim (\beta/\epsilon_b)|\mathcal{M}_2|$ characteristically.

2.4 Numerical Solutions

2.4.1 Field Line Structure

In the strong Type II limit where $H = H_{c1}(\rho)$ does not depend on B, we can solve (2.17) and (2.19) for each magnetic field line individually. Symmetry dictates that field lines be vertical at their equatorial footpoints. For the "most dipolar" solutions that match to a pure dipole field in the normal shell to zeroth order in ℓ and β, we also require that each field line be vertical at x_b. We can label each field line by its footpoint radius, x_0. Once we specify $H(\rho) = H_{c1}(\rho)$ we can find the value of $\hat{\mathcal{J}}(x_0)$ for which these conditions are satisfied. Thus, we determine both the source and the field line shapes that are consistent with our boundary conditions.

In order to choose the function $H(\rho)$ we fit the values of the proton fraction given in Zuo *et al.* [3] to power laws of the baryon density. Writing $H(\rho) \propto \rho^b$, we found that $b \approx 1.6-1.8$. We used the $N = 1$ polytrope for the mass density profile of the star.

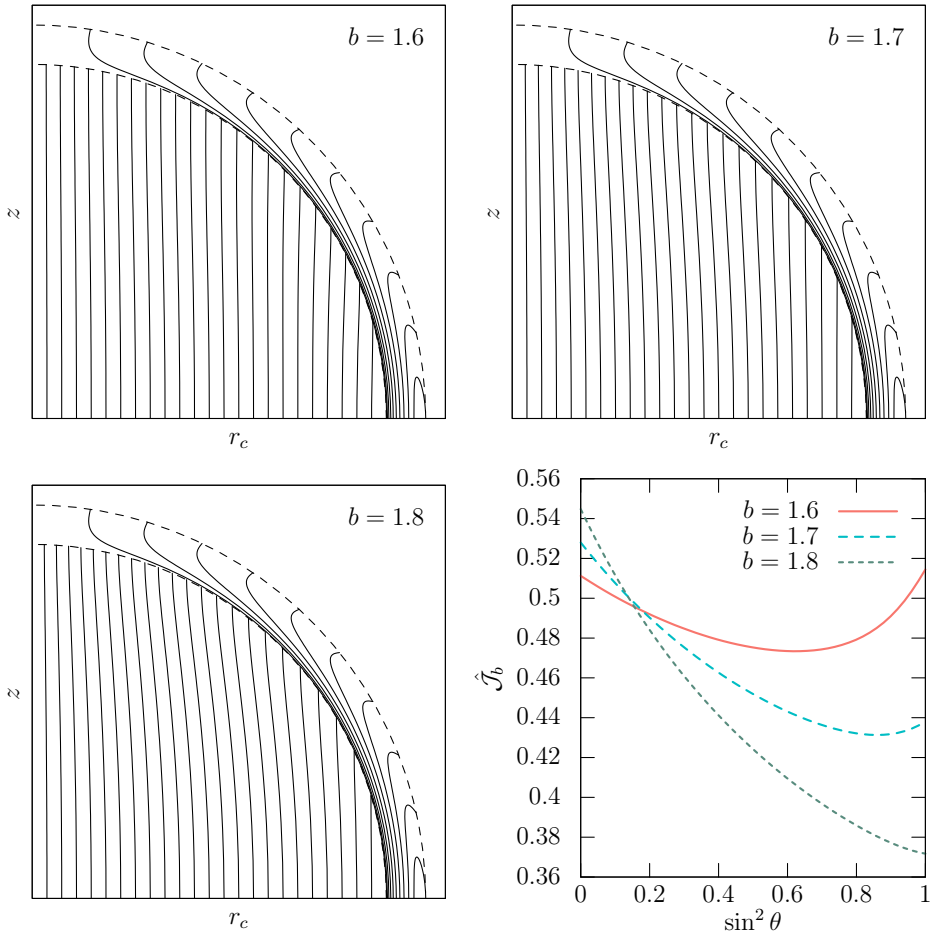

Figure 2.3: Field line configurations assuming $H(\rho) \propto \rho^b$ with $b = 1.6$, 1.7 and 1.8. The inner and outer dashed lines show the boundary of the Type II core at $r = 0.9R$ and the stellar surface at $r = R$, respectively, for the stellar magnetic axis in the z direction. The lower right panel shows the value of the rescaled current parameter $\hat{\mathcal{J}}$ as a function of $\sin^2\theta$ along the inner dashed boundary.

Figure 2.3 shows the results for $b = 1.6$, 1.7 and 1.8. Note that there are two competing features of the solutions: $\boldsymbol{\nabla} H$ tends to curve the field lines inward, and $\hat{\mathcal{J}}(x_0)$ opposes this trend. The field lines are most nearly vertical throughout the core for $b = 1.6$, the smallest value displayed. Even though the field line shapes are not precisely vertical throughout the core, the deviations are relatively small. We have also found the field line solutions for $b = 1$, 1.5, and 2; they are substantially similar to the configurations shown in figure 2.3.

The lower right panel shows the current density parameter $\hat{\mathcal{J}}_b$ as a function of $\sin^2\theta$. This quantity is found by determining $\hat{\mathcal{J}}(x_0)$ for each field line; using the solution for $\theta(\sigma)$ along the line, we find where it intersects the surface x_b. Note that our solutions *do not* determine the value of A for a given field line.

For $B = 0 = \beta$ and $\ell = 0$ boundary conditions at the core-shell interface dictate that $\boldsymbol{B} = -H_b \sin\theta\,\hat{\boldsymbol{\theta}}$ at the base of the shell. This means that in this approximation field lines *do not* penetrate from the core to the shell. The solution inside the shell that matches smoothly to a vacuum field is given by (2.26). Since there are two boundary conditions at x_b, the surface boundary condition determines $\hat{\mathcal{J}}_{\rm shell}$ (see (2.27)) so the entire solution outside the core not only is determined fully but also depends on H_b.

Figure 2.4 illustrates the field line configuration for $b = 1.6$ but $\beta = 0.1$, to lowest order in β. (Corrections will be considered in section 2.4.3.) In this case, field lines from the core penetrate into the normal shell. The inner thick line shows the bounding field line. It is apparent that field lines hug close to $x = x_b$ before fanning out into a polar cap whose angular extent is $\sim\sqrt{\beta}$. Also shown in this figure is the small region where field lines in the shell are closed: the first open field line has its inner footpoint at $x \simeq 0.97\pi$. (This region is also apparent in the $\beta = 0$ configurations in figure 2.3.) In a fluid shell, this region would be magnetohydrodynamically unstable [45, 46] but shear stresses in the normal shell restore stability since the shear modulus $\mu \gg B^2 \sim 10^{24} B_{12}^2\,{\rm g\,cm^{-1}\,s^{-2}}$ [e.g. 36, 47, 48].

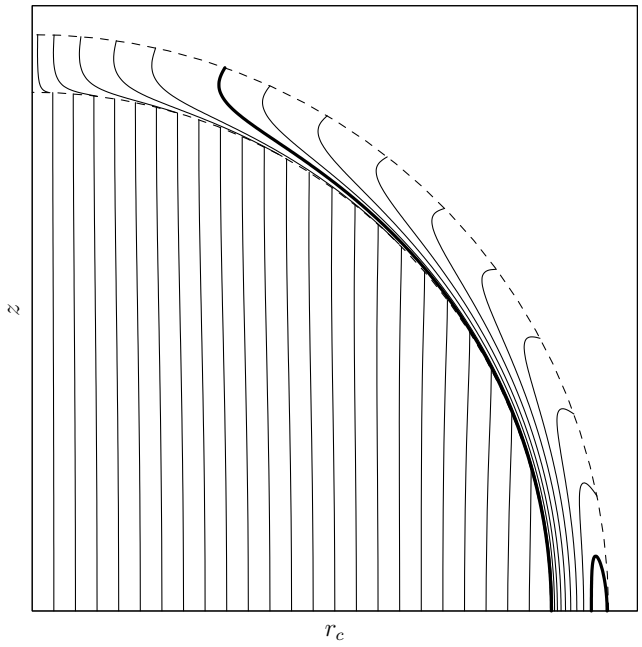

Figure 2.4: Field line configuration in the same layout as in figure 2.3, with nonzero B field strength at the core boundary. Shown here is the case where $\beta = 0.1$, as defined in (2.35), and $b = 1.6$. Field lines in the shell are computed to lowest order in β; for corrections see section 2.4.3.

2.4.2 Magnetic Distortion: Mass Quadrupole Moment

In general, there are four contributions to the quadrupolar distortion to linear order in B/H_b:

$$\mathcal{M}_2 = -10^{-9} H_{b,14}^2 R_{10}^2 M_{1.4}^{-2} \left[C_1 + (C_2 + C_3 + C_4) \frac{B}{H_b} \right] \ . \tag{2.54}$$

The coefficients C_1 and C_2 arise from the shell, and are independent of the core structure; for $r_b = 0.9R$, $(C_1, C_2) = (+1.58, +28.3)$. The coefficient C_3 arises from $\Phi(A)$ and the coefficient

C_4 arises from $B\partial f/\partial\rho$; these depend on the structure of the core field: for $r_b = 0.9R$

$$(C_3, C_4) = \begin{cases} (+30.4, -0.434) & \text{if } b = 1.6 \\ (+35.4, -2.20) & \text{if } b = 1.7 \\ (+40.7, -4.64) & \text{if } b = 1.8 \\ (+36.7, 0) & \text{Toy} \end{cases} \tag{2.55}$$

where in all cases $C_3 > |C_4|$ because field lines are nearly vertical (exactly vertical in the toy model). Roughly speaking, the coefficient of B/H_b in (2.54) is $\simeq 60$, but $B/H_b \approx 2f(\pi; x_b)R^2\beta/3\pi^2 r_b^2 = \beta/14.1$ for $r_b = 0.9R$, which mitigates the dependence of $\mathcal{M}_2$ on B for small β.

2.4.3 Perturbative Corrections: Nonzero ℓ and β

Table 2.1 shows the results of computing perturbations resulting from nonzero transition zone thickness using the method developed in appendix 2.A.1. Although the table only contains results for multipoles Q_j with $j \leq 5$, the calculations were performed using $\hat{\mathcal{J}}_{b,j}$ with $j \leq 14$, and therefore determined Q_j for $j \leq 14$. The procedure can be iterated but we did not do so. To obtain these results, we solved (2.67) with $\Delta A_j(x_b) = 0$. Appendix 2.B shows that in fact $\Delta A_j(x_b) \neq 0$. However, according to (2.81), $\Delta A_j(x_b)$ is primarily dipolar to $\mathcal{O}(\ell)$. This dipolar component as well as the effect of $\hat{\mathcal{J}}_{b,0}$ may be absorbed into a "renormalized" background solution. The second line in table 2.1 tabulates the "extra" change in Q_0 that results when we renormalize in this fashion.

Table 2.1 shows that the multipole perturbations that result from nonzero ℓ are small but not entirely negligible. For example, the shift in the dipole moment is $\Delta\mu/\mu = -17.01\ell/R$; for $\ell/R = 0.01$ this is a downward change of about 17%. Since we require $\Delta A_j(x_b)$ to be relatively small, (2.81) indicates that $\ell/R \ll B/H_b \sim \beta\epsilon_b$, so consistency would require somewhat smaller $-\Delta\mu/\mu$: shifts are restricted to $\lesssim$ a few percent. The other multipole

j	$\hat{\mathcal{J}}_{b,j}$	$Q_j(\ell)/R^{2j-1}\ell\mu$
0	-4.918×10^{-1}	$1.701\times10^{\ 1}$
0	0	5.239×10^{-1}
1	6.067×10^{-3}	-4.999×10^{-1}
2	-5.198×10^{-3}	2.723×10^{-1}
3	1.241×10^{-3}	-6.844×10^{-2}
4	-3.843×10^{-4}	1.973×10^{-2}
5	8.526×10^{-5}	-3.657×10^{-3}

Table 2.1: Values of $\hat{\mathcal{J}}_{b,j}$ (col. 2), $Q_j(\ell)/R^{2j}\ell\mu$ (col. 3) for $j \le 5$ (col. 1) and $b = 1.6$ and $r_b = 0.9R$. Second line renormalizes H_b as described in the text.

moments are smaller by at least a factor of 30.

Implementing the procedure in appendix 2.A.2 proved more challenging computationally, particularly for larger values of β, where the various matrices that had to be inverted turned out to be nearly singular. These computational problems did not arise for $\beta \le 0.05$, and for $10^{-5} \le \beta \le 0.05$ we found $\Delta\mu/\mu \simeq -0.115\beta$ and a RMS change $\Delta A_{\rm rms}(R)/A_0(R) \simeq 0.150\beta$ assuming $b = 1.6$ and $\epsilon_b = 0.1$. Thus, although the perturbations are predominantly dipolar, nondipole contributions are only a few times smaller. These results were found using various maximum $0 \le j_{\rm in} \le 10$ in the expansion for $\hat{\mathcal{J}}_b(\theta)$, and various maximum $10 \le j_{\rm max} \le 14$ in the multipole expansion within the normal shell. Empirically, we found that about 90% of the perturbation arose when we took $j_{\rm in} = 0$, which suggests that the main effect arises from the peculiar shape of the region within the shell occupied by field lines entering from the Type II core; see figure 2.4.

2.5 Discussion and Conclusions

In this paper, we developed the formalism for computing the configuration of poloidal magnetic fields inside a neutron star with a strongly Type II superconducting core. Qualitatively, the restriction to hydrostatic balance without "magnetic buoyancy" imposes constraints on the electric current density given by (2.10). Because of these constraints, we must determine

both the current densities and field line structure at the same time. Within the Type II core, the task is simplified when $B \ll H$, for in this limit H is a function of density, and therefore a function of radius, to lowest order in the magnetic distortion.

The main results of this paper are:

1. The Type II core provides an important boundary condition for fields in the normal shell surrounding it; see (2.25).

2. If the core is strongly Type II, continuity of the tangential and normal components of magnetic field imply that the field points very nearly along the inner boundary of the normal shell, unless the field just inside the boundary is tuned finely. Thus, generically field lines from the core do not penetrate deep into the normal shell of the star. However, the field strength at the base of the normal shell is $\sim H_b$ in this case.

3. Substantial currents in the normal shell are required for the field to adjust in strength and direction to conform with vacuum boundary conditions at the radius of the star.

4. In the "most dipolar case" in which the field is vertical at the outer edge of the Type II core, the emerging field is dipolar, with a surface field strength given by (2.26).

5. If the thickness of the normal shell of the star is $\epsilon_b R$ with $\epsilon_b \ll 1$, the surface field strength for the "most dipolar" case is $\simeq H_b\epsilon_b/3$. For typical neutron star parameters (2.4) implies a surface field strength $\simeq 3 \times 10^{12}$ G, which is characteristic of the large population of "normal neutron stars."

6. Magnetic fields induce a quadrupolar distortion of the star $\mathcal{M}_2 \simeq -10^{-9}$. The scale of the distortion is set primarily by H_b for small B/H_b; see (2.54).

7. Perturbations arise from the finite thickness of the transition layer in which the superconductor disappears and from field lines that penetrate from the Type II core to the

normal shell. These perturbations are small if $\ell/\epsilon_b R \ll \beta \ll 1$, which delineates the domain of validity of our calculations.

Although our calculations assume a star in hydrostatic balance, some of the qualitative features found here would hold for stars that are out of equilibrium as well. For example, in configurations without surface currents, we would still expect field lines to emerge from the core pointing largely along the inner boundary of the normal shell, with a field strength there $\sim H_b$. Consequently, we would still expect the emerging field to have a field strength similar to what is found in equilibrium.

Our calculations have employed a very simple equation of state: the $N = 1$ polytrope. Within the context of this equation of state, if we stipulate that ρ_b is fixed by microphysics of the phase change from core fluid with free protons to a crystalline crust with protons confined to nuclei, then H_b will be independent of the stellar mass. However, since R is fixed for a (Newtonian) $N = 1$ polytrope the central density is $\propto M$ and the fractional thickness of the normal shell is $\propto 1/M$. Thus, we would expect some variation of the surface magnetic field with stellar mass, but this would only lead to a rather small range of values differing by less than a factor of two.

More realistically, with H_b fixed the surface field strength will still be $\propto H_b\epsilon_b$, but the value of ϵ_b and the proportionality constant would depend on details of the equation of state. We expect this to remain so even if the Type II region does not encompass the entire stellar core, as we have assumed here: Type II superconductor with an inner boundary would have different currents but the lower boundary condition on the normal shell is sensitive primarily to H_b. Nevertheless, very generally we expect that the "most dipolar" case will result in field strengths $\sim 10^{12}$ G with little variation. This is contrary to observations, which show that even the dipolar field strengths, as indicated by the $P - \dot{P}$ diagram for radiopulsars [e.g. 49], vary over several orders of magnitude.

The obvious solution to this problem is that the magnetic field configurations for many

pulsars are very similar to the most dipolar configuration, but that there may be substantial deviations. We envision several reasons for such variation:

1. The strong Type II limit fails because $B \sim H$ in the core. We expect that this is true for magnetars, for example.

2. Failure of the strong Type II limit is an extreme example of a case that is outside the scope of the calculations in this paper. There are configurations with $B \ll H_b$ that violate our requirements: (a) If $\epsilon_b^{-1} \gg \beta \gtrsim 1$ field lines impinging from the core affect the surface field non-perturbatively. (b) If β is small enough that $\ell/R \gtrsim B/H_b \sim \beta\epsilon_b$ then field lines curve significantly within the transition region between the Type II core and normal shell, which would affect their coupling.

3. Toroidal magnetic fields, which were not considered here, can alter the poloidal field configuration even in hydrostatic equilibrium. We will treat this possibility elsewhere. Toroidal fields also mitigate instability. We have seen that there is a region in the normal shell that would be unstable if the normal shell were a pure fluid (see figure 2.4) although in a crystalline crust shear stresses should suffice to ensure stability there. However, the Muzikar-Pethick-Roberts instability in the Type II core [10, 11, 50] might require toroidal fields to ensure stability.

4. Even if none of the last three caveats holds, so the core is in the strong Type II regime and toroidal fields do not affect the poloidal fields significantly, the requirement that field lines hit the outer boundary of the Type II core vertically that is the basis for the most dipolar configuration is very special. Relaxing it could lead to greater diversity in surface field strengths.

We expect that of these options the last is most important for neutron stars with surface magnetic field strengths substantially below 10^{12} G. The extreme case is when field lines

hit the outer boundary of the Type II core radially. The field line configuration within the core is shown in figure 2.1, panel A. In this extreme, the field remains radial as it enters the normal shell, and is weak in strength, $\sim B \ll H_b$. Entering field lines carry current density $\sim c\rho_b H(0)/\rho(0)R$ with them, and therefore curve downward toward the stellar equator within a short distance of the boundary: crudely the field should penetrate a distance $\sim B\rho(0)R/\rho_b H(0)$, which is $\sim \beta(\rho_b/\rho(0))^{b-1} \ll 1$ times the thickness of the shell. We might then expect that the entering field lines are confined to a small region of the normal shell, and the field strength at the surface could be $\lesssim B\epsilon_b$, which may be very small. We will report elsewhere on calculations that employ different boundary conditions at the outer radius of the Type II core.

Even though it relies on special conditions, the "most dipolar" solution reveals that there is a characteristic surface magnetic fields strength that is determined by the nuclear equation of state. Our calculations show that this field strength is $\sim 10^{12}$ G, reassuringly close to the values deduced for many neutron stars. By relaxing the restrictive boundary conditions underlying the most dipolar solution, it seems plausible that a variety of field strengths may be attained in equilibrium. Field strengths $\gg 10^{12}$ G or $\ll 10^{12}$ G may be attained under other restrictive conditions.

Acknowledgements

We thank S. Lander and A. Sedrakian for helpful correspondence. This research was supported in part by NSF grant AST-0606710, NSF grant PHY11-25915, by a fellowship from the NASA/New York Space Grant Consortium and by the College of Arts and Sciences, Cornell University.

2.A Perturbation Solutions

We begin with a zeroth order solution, $A_0(x,\theta)$, that corresponds to a given $\hat{\mathcal{J}}_{\rm shell}(A)$; we use (2.26). Perturbations distort the solution to

$$A(x,\theta) = A_0(x,\theta) + \sin\theta \sum_{J=0}^{\infty} \Delta A_j(x) {P_{2j+1}}^1(\cos\theta) \ . \tag{2.56}$$

The perturbed solution corresponds to $\hat{\mathcal{J}}(A) = \hat{\mathcal{J}}_{\rm shell} + \Delta\hat{\mathcal{J}}(A)$, where $\Delta\hat{\mathcal{J}}(A)$ must be determined along with the perturbed field solution. To do this, we begin by choosing a functional form for $\Delta\hat{\mathcal{J}}(A)$ which will necessarily involve unknown parameters to be determined. Since $A \approx A_0$ by assumption, we substitute $\Delta\hat{\mathcal{J}}(A) \approx \Delta\hat{\mathcal{J}}(A_0)$ to find the perturbed field; because A_0 is known we may expand

$$\sin\theta \Delta\hat{\mathcal{J}}(A_0) = \sum_{j=0}^{\infty} S_j(x) {P_{2j+1}}^1(\cos\theta) \tag{2.57}$$

to get the equation

$$\frac{d^2\Delta A_j}{dx^2} - \frac{(2j+1)(2j+2)\Delta A_j}{x^2} = -\frac{H(0)R^2 x \sin x S_j(x)}{\pi^2} \ , \tag{2.58}$$

which, with the boundary condition $x d\Delta A_j/dx + (2j+1)\Delta A_j = 0$, has the solution

$$\begin{aligned} \Delta A_j(x) \ = \ & \frac{\Delta A_j(x_b) x_b^{2j+1}}{x^{2j+1}} + \frac{H(0)R^2}{(4j+3)\pi^2}\left[x^{2j+2}\int_x^\pi \frac{dx' \sin x' S_j(x')}{(x')^{2j}} \right. \\ & \left. - \frac{x_b^{4j+3}}{x^{2j+1}}\int_{x_b}^\pi \frac{dx' \sin x' S_j(x')}{(x')^{2j}} + \frac{1}{x^{2j+1}}\int_{x_b}^x dx' (x')^{2j+3} \sin x' S_j(x') \right] \ . \end{aligned} \tag{2.59}$$

Differentiating (2.59) and evaluating at x_b implies

$$-\frac{R^2\Delta B_{\theta,j}(x_b)}{\pi^2} = \left(\frac{1}{x}\frac{d\Delta A_j}{dx}\right)_{x_b} = -\frac{(2j+1)\Delta A_j(x_b)}{x_b^2} + \frac{H(0)R^2 x_b^{2j}}{\pi^2}\int_{x_b}^{\pi}\frac{dx'\sin x' S_j(x')}{(x')^{2j}} \tag{2.60}$$

where the perturbed field tangential to the boundary at x_b is

$$\Delta B_\theta(x_b,\theta) = \sum_{j=0}^{\infty}\Delta B_{\theta,j}(x_b) {P_{2j+1}}^1(\cos\theta)\ . \tag{2.61}$$

Equation (2.60), given (2.61), is used to determine the unknown parameters of the source term, $\Delta\hat{\mathcal{J}}(A)$. Once these parameters have been found, (2.59) evaluated at $x=\pi$ determines the multipole moments $Q_j = \Delta A_j(\pi)R^{2j+1}$:

$$Q_j = \Delta A_j(x_b) r_b^{2j+1} + \frac{H(0) r_b^{2j+3}}{4j+3}\int_{x_b}^{\pi} dx'\sin x' S_j(x')\left[\left(\frac{x'}{x_b}\right)^{2j+3} - \left(\frac{x_b}{x'}\right)^{2j}\right]\ . \tag{2.62}$$

Non-trivial perturbations will always engender multipole fields at the surface.

2.A.1 Surface Currents from Transition Layer

We write the zeroth order solution as $A_0 = A_s\tilde{f}(x;x_b)\sin^2\theta$, where $A_s = F_0(\pi)$ so $\tilde{f}(\pi;x_b) = 1$, and expand

$$\Delta\hat{\mathcal{J}}(A) = \sum_{j=0}^{j_{\max}}\Delta\hat{\mathcal{J}}_n\left(\frac{A}{A_s}\right)^n \approx \sum_{J=0}^{j_{\max}}\Delta\hat{\mathcal{J}}_n(\sin\theta)^{2n}[\tilde{f}(x;x_b)]^n \tag{2.63}$$

where we substituted $A\approx A_0$; then

$$\begin{aligned}\mathcal{S}_j(x) &= \sum_{n=j}^{j_{\max}}\frac{N_{nj}\Delta\hat{\mathcal{J}}_n[\tilde{f}(x;x_b)]^n}{N_j}\ ,\\ N_{nj} &= \frac{2\pi\Gamma(n+2)\Gamma(n+1)}{\Gamma(n+j+\frac{5}{2})\Gamma(n-j+1)\Gamma(j+1)\Gamma(-j-\frac{1}{2})}\end{aligned} \tag{2.64}$$

For sufficiently small transition region thickness ℓ the jump condition from Type II core to normal shell is given by (2.29), and therefore

$$\Delta B(x_b, \theta) = \frac{\pi \ell \hat{\mathcal{J}}_b(\theta) H(0) \sin x_b \sin \theta}{R} \tag{2.65}$$

where $\hat{\mathcal{J}}_b(\theta)$ is the current density parameter at the outer edge of the Type II core, which we compute for each field line; then with

$$\sin\theta \hat{\mathcal{J}}_b(\theta) = \sum_{j=0}^{\infty} \hat{\mathcal{J}}_{b,j} {P_{2j+1}}^1(\cos\theta) \tag{2.66}$$

(2.60) becomes

$$-\frac{\pi \ell \hat{\mathcal{J}}_{b,j} \sin x_b}{R} + \frac{(2j+1)\Delta A_j(x_b)}{H(0) r_b^2} = \sum_{n=j}^{j_{\max}} \frac{N_{nj} \Delta \hat{\mathcal{J}}_n}{N_j} \int_{x_b}^{\pi} \frac{dx \sin x [\tilde{f}(x; x_b)]^n}{(x/x_b)^{2j}} \ , \tag{2.67}$$

which is a linear equation for the $\Delta \hat{\mathcal{J}}_n$. The multipole moments are then found by combining (2.62), (2.64) and the solution of (2.67).

2.A.2 Field Lines Poking in from the Core

We do not know $A(x_b, \theta)$ *a priori*. In the strong Type II core, field lines are labelled by their foot points x_0, and our solutions determine (i) the value of θ where they hit the boundary and (ii) the value of $\hat{\mathcal{J}}_b(\theta)$ there, subject to whatever constraint we impose on the solution, such as for the "most dipolar" solution. We need $A(x_b, \theta)$ in order to map $\hat{\mathcal{J}}_b(\theta) \to \hat{\mathcal{J}}_{\rm core}(A)$, which is needed to determine the effect of impinging field lines on the normal shell solution.

$\boldsymbol{A(x_b, \theta) = \frac{1}{2} B r_b^2 \sin^2 \theta}$

In this case, the background solution is (2.31) with current parameter (2.32). We take $\Delta B_j(x_b) = 0 = \Delta A_j(x_b)$.

A key feature of this background solution is that field lines from the Type II core penetrate into the normal shell, bringing along the currents $\hat{\mathcal{J}}_{\rm II}(A) = \hat{\mathcal{J}}_b(\theta(A))$ associated with them, where $\theta(A) = \sin^{-1}(\sqrt{2A/Br_b^2})$. Defining $\Delta\hat{\mathcal{J}}_{\rm II}(A) = \hat{\mathcal{J}}_{\rm II}(A) - \hat{\mathcal{J}}_{\rm shell}(B)$ we have

$$\begin{aligned}\Delta\hat{\mathcal{J}}(A) &= \Delta\hat{\mathcal{J}}_{\rm II}(A)\Theta(\frac{1}{2}Br_b^2 - A) + \Delta\hat{\mathcal{J}}_{\rm shell}(A)\Theta(A - \frac{1}{2}Br_b^2) \\ &\approx \Delta\hat{\mathcal{J}}(A_0)\Theta(\theta_{\rm II}(x) - \theta) + \Delta\hat{\mathcal{J}}_{\rm shell}(A_0)\Theta(\theta - \theta_{\rm II}(x)) \ , \end{aligned} \tag{2.68}$$

where the second line assumes $A \approx A_0$, and

$$\begin{aligned}S_j(x) = \frac{2}{N_j}\Bigg[&\int_{\cos\theta_{\rm II}(x)}^{1} d\mu\sqrt{1-\mu^2}\Delta\hat{\mathcal{J}}_{\rm II}(A_0){P_{2j+1}}^1(\mu) \\ &+ \int_0^{\cos\theta_{\rm II}(x)} d\mu\sqrt{1-\mu^2}\Delta\hat{\mathcal{J}}_{\rm shell}(A_0){P_{2j+1}}^1(\mu)\Bigg] \ . \end{aligned} \tag{2.69}$$

Generically, the first term in (2.69) is $\mathcal{O}(1)$ for $x - x_b \lesssim \beta\epsilon_b$ and is $\mathcal{O}(\beta^2)$ for $x - x_b \sim \epsilon_b$. To find $\Delta\hat{\mathcal{J}}_{\rm shell}(A)$ we must first specify its functional form and then determine the associated parameters from (2.60) with $\Delta B_{\theta,j}(x_b) = 0$; the generic scalings suggest that $\Delta\hat{\mathcal{J}}_{\rm shell}(A) = \mathcal{O}(\beta)$. If we expand

$$\Delta\hat{\mathcal{J}}_{\rm II} = \sum_{n=0}^{j_{\rm max}} \Delta\hat{\mathcal{J}}_{n,{\rm II}} \sin^{2n}\theta \tag{2.70}$$

on x_b, with *known* coefficients $\{\Delta\hat{\mathcal{J}}_{n,{\rm II}}\}$ and $\Delta\hat{\mathcal{J}}_{\rm shell}(A)$ as in (2.63) with *unknown* coefficients $\{\Delta\hat{\mathcal{J}}_{n,{\rm shell}}\}$

$$\begin{aligned}S_j(x) &= \frac{1}{N_j}\sum_{n=0}^{j_{\rm max}}\left\{\mathcal{N}_{n,j}(x)\Delta\hat{\mathcal{J}}_{n,{\rm II}} + \left[\frac{N_{nj}[\beta x_b/x + \tilde{f}(x;x_b)]^n - \beta^n\mathcal{N}_{n,j}(x)}{(\beta r_b/R+1)^n}\right]\Delta\hat{\mathcal{J}}_{n,{\rm shell}}\right\} \\ \mathcal{N}_{n,j}(x) &\equiv \frac{2}{\sin^{2n}\theta_{\rm II}(x)}\int_{\cos\theta_{\rm II}(x)}^{1} d\mu(1-\mu^2)^{n+1/2}{P_{2j+1}}^1(\mu) \ ; \end{aligned} \tag{2.71}$$

although $N_{nj} = 0$ for $j > n$, $\mathcal{N}_{n,j}(x) \neq 0$ in general. The $\{\Delta\hat{\mathcal{J}}_{n,\rm shell}\}$ are the solution of

$$\begin{aligned} 0 &= \sum_{n=0}^{j_{\max}} \left(\Delta\hat{\mathcal{J}}_{n,\rm II} - \frac{\beta^n \Delta\hat{\mathcal{J}}_{n,\rm shell}}{(\beta r_b/R+1)^n} \right) \int_{x_b}^{\pi} \frac{dx \sin x \mathcal{N}_{n,j}(x)}{(x/x_b)^{2j}} \\ &\quad + \sum_{n=j}^{j_{\max}} N_{nj} \Delta\hat{\mathcal{J}}_{n,\rm shell} \int_{x_b}^{\pi} \frac{dx \sin x [\beta x_b/x + \tilde{f}(x;x_b)]^n}{(x/x_b)^{2j}(\beta r_b/R+1)^n} \ . \end{aligned} \tag{2.72}$$

General $A(x_b, \theta)$

We can incorporate more complicated $A(x_b, \theta)$; let

$$A(x_b,\theta) = \frac{1}{2} B r_b^2 \left[\sin^2\theta + \sin\theta \sum_{j=1}^{\infty} a_j {P_{2j+1}}^1(\cos\theta) \right] \ ; \tag{2.73}$$

the coefficients $\{a_j\}$ may be derived from a given $A(x_b, \theta)$ via inversion. Equation (2.73) implies a different mapping $\theta(A)$ on x_b, hence a different form of $\hat{\mathcal{J}}_{\rm II}(A)$ for impinging field lines. With (2.73), the background solution is multipolar. The $j = 0$ component is (2.31) but the other multipoles are generically

$$\begin{aligned} A_j(x) &= \frac{B r_b^2 a_j x_b^{2j+1}}{2x^{2j+1}} + \frac{H(0)R^2}{(4j+3)\pi^2} \left[x^{2j+2} \int_x^{\pi} \frac{dx' \sin x' S_j^{(0)}(x')}{(x')^{2j}} \right. \\ &\quad \left. - \frac{x_b^{4j+3}}{x^{2j+1}} \int_{x_b}^{\pi} \frac{dx' \sin x' S_j^{(0)}(x')}{(x')^{2j}} + \frac{1}{x^{2j+1}} \int_{x_b}^{x} dx' (x')^{2j+3} S_j^{(0)}(x') \right] . \end{aligned} \tag{2.74}$$

The current density in this model is $\hat{\mathcal{J}}_{\rm shell} + \hat{\mathcal{J}}^{(0)}(A)$, where $\hat{\mathcal{J}}^{(0)}(A)$ must be determined. Because the impinging fields are weak compared with H_b, we can determine the currents perturbatively via the analogues of (2.57), (2.63) and (2.64), plus the analogue of (2.60) with the condition $\Delta B_j(x_b) = 0$.

Once the full background solution has been found, the boundary of the region to which impinging field lines are confined may be determined. We can then proceed as in section 2.A.2 to find the perturbation to the background solution. Equation (2.73) implies a total flux

$A(x_b, \pi/2)$ through the upper hemisphere. Consistency of the perturbation theory requires $A(x_b, \pi/2) << H_b R^2 \epsilon_b$.

2.B The Thin Shell Approximation for the Transition Layer

The proton density plummets in a thin layer that extends from $r = r_b$ to $r = r_b + \ell$; let $r = r_b + \ell s$. As n_p falls, so does Δ_p and the superconductor disappears. For small enough $p_{F,p}$, nonzero temperature will matter: for $\Delta_p \sim T$, the superconductor may first become Type I before disappearing entirely at $p_{F,p} \neq 0$. Our treatment here assumes that $T \neq 0$ is only important in a very thin subdomain of the transition layer that has little effect on the magnetic field. With $\Delta_p \propto p_{F,p}^2$ at small $p_{F,p}$ for $T = 0$ [e.g. 51] (2.1) implies $\kappa \propto p_{F,p}^{-1/2}$, so the superconductor remains Type II. However, as k_L shrinks interactions among field lines become increasingly important; if $H_{c1}(\rho) = H_{c1}(s)$ within the layer, then the magnetic field strength is

$$H = H_{c1}(s) + Bf\left(\sqrt{\frac{H_{c1}(s)}{B}}\right) \tag{2.75}$$

where $H_{c1}(s)$ is given by (2.3) and $f(0) = 1$ and $f(z) \to 0$ exponentially as $z \to \infty$. Ampére's law is

$$\frac{\pi \ell \sin x_b H(0) \hat{\mathcal{J}}(A) \sin\theta}{R} = \frac{\partial H_\theta}{\partial s} + \frac{\ell}{r}\left(H_\theta - \frac{\partial H_r}{\partial \theta}\right) \ ; \tag{2.76}$$

if we assume that field lines do not rotate significantly, so that we can identify A with θ, and only retain the lowest order in ℓ, (2.76) implies

$$-H_\theta(s,\theta) \simeq \left[H_b - \frac{\pi \ell s \sin x_b H(0) \hat{\mathcal{J}}(A)}{R}\right] \sin\theta \ . \tag{2.77}$$

The magnetic induction field is

$$\boldsymbol{B} = -\frac{\hat{\boldsymbol{\theta}}}{\ell r \sin\theta}\frac{\partial A}{\partial s} + \frac{\hat{\boldsymbol{r}}}{r^2 \sin\theta}\frac{\partial A}{\partial \theta} \ ; \tag{2.78}$$

in the thin layer approximation we assume that B_r remains constant and therefore $B_\theta = \pm\sqrt{1 - B_r^2/B^2}$. We assume that H_θ (and B_θ) remain in the $-\hat{\boldsymbol{\theta}}$ direction, so

$$\left[H_b - \frac{\pi \ell s \sin x_b H(0)\hat{\mathcal{J}}(A)}{R}\right]\sin\theta \simeq \sqrt{1 - \frac{B_r^2}{B^2}}\left[H_{c1}(s) + Bf\left(\sqrt{\frac{H_{c1}(s)}{B}}\right)\right] \ , \tag{2.79}$$

which is an algebraic equation for B. Once B is found from (2.79), we can solve for the change in A:

$$\frac{\partial A}{\partial s} \simeq \ell r_b \sin\theta \sqrt{B^2 - B_r^2} \ . \tag{2.80}$$

Ultimately, B approaches (2.77), hence the change in $A(s,\theta)$ across the layer is

$$\Delta A(\theta) = A(1,\theta) - A(0,\theta) \simeq \ell r_b \sin^2\theta \left[H_b - \frac{\pi \ell \sin x_b H(0)\hat{\mathcal{J}}(A)}{2R}\right] \ . \tag{2.81}$$

Equation (2.81) shows that $\Delta A(\theta)$ is relatively small provided that $\ell H_b/Br_b \ll 1$.

3 | Initial data for high-compactness black hole–neutron star binaries[1]

Abstract

For highly compact neutron stars, constructing numerical initial data for black hole–neutron star binary evolutions is very difficult. We describe improvements to an earlier method that enable it to handle these more challenging cases. We examine the case of a 6:1 mass ratio system in inspiral close to merger, where the star is governed by a polytropic $\Gamma = 2$, an SLy, or an LS220 equation of state. In particular, we are able to obtain a solution with a realistic LS220 equation of state for a star with compactness 0.26 and mass $1.98\,\mathrm{M}_\odot$, which is representative of the highest reliably determined neutron star masses. For the SLy equation of state, we can obtain solutions with a comparable compactness of 0.25, while for a family of polytropic equations of state, we obtain solutions with compactness up to 0.21, the largest compactness that is stable in this family. These compactness values are significantly higher than any previously published results. We find that improvements in adapting the computational domain to the neutron star surface and in accounting for the center of mass drift of the system are the key ingredients allowing us to obtain these solutions.

[1]Submitted for publication in *Class. Quantum Grav.*; preprint at arXiv:1409.7159 [gr-qc].

3.1 Introduction

Among the prime candidate sources for ground-based gravitational wave detectors are binary systems containing inspiraling neutron stars: black hole–neutron star (BHNS) binaries, or systems containing two neutron stars. Besides being likely gravitational wave sources, such systems are the leading candidates to explain short gamma-ray bursts [52–56]. Radioactive decay of the neutron-rich material ejected by the merger may also power optical/infrared transients days after the merger [57–59], particularly for BHNS binaries with a large neutron star and a rapidly rotating black hole [60–64], and for binary neutron star mergers with compact neutron stars [65].

Gravitational waves from coalescing binaries are searched for and analyzed using the matched-filtering technique [66–69], which compares the detector output with a bank of templates that model the waves emitted by the source. Therefore accurate knowledge of the expected waveforms of incoming signals is required. While post-Newtonian templates are expected to be accurate when the binary is widely separated, they break down near merger. Fully relativistic numerical simulations of the last few orbits and the merger are needed to match onto the post-Newtonian waveforms. Moreover, modeling of the subsequent electromagnetic and neutrino emission must also be done by a code that can deal with all the effects of strong-field gravity.

Numerical modeling of these systems is very challenging (see [18, 19, 70, 71] for reviews). A key ingredient in such simulations is accurate initial data. Ideally, one would like a snapshot of the gravitational field and the matter distribution only a few orbits before merger but resulting from millions of years of slow inspiral. In general relativity, no exact way is known to do this because the nonlinear Einstein equations are too difficult to solve. So instead, various plausible approximations are made. The most common assumption is that the binary has had time to settle into a quasi-equilibrium state, the system being

approximately time-independent in the corotating frame. Furthermore, as the viscous forces within the star are expected to be small, we do not expect much change in the spin of the star as the orbital radius decreases. For an initially nonspinning neutron star, this would lead to an irrotational velocity profile, another standard assumption. Because of gravitational wave emission, however, there is no exact equilibrium state. Accordingly, these conditions cannot all be perfectly satisfied simultaneously. Nevertheless, initial data incorporating these assumptions seems to work quite well in practice.

This paper will focus on initial data for BHNS binaries, and in particular systems where the neutron star has high compactness

$$\mathcal{C} = \frac{M_{\rm NS}}{R}. \tag{3.1}$$

Here $M_{\rm NS}$ is the ADM mass and R is the areal radius for an isolated star with the same equation of state and baryon mass, and we use units with $c = G = 1$. The techniques introduced here should be equally applicable to neutron star–neutron star binaries.

Previous results on initial data for BHNS evolutions include the early work of Taniguchi *et al.* [72] and Sopuerta *et al.* [73], as well as more recent initial configurations generated by Taniguchi *et al.* [74–76] and Grandclément [77]. Both Taniguchi and Grandclement use codes based on the LORENE package [78], and excise from the computational domain the region inside the apparent horizon of the black hole. An alternative method based on the puncture formalism, in which the constraints are solved both inside and outside the black hole horizon, has been proposed by Kyutoku *et al.* [79]. The results from [79] were also obtained using LORENE. A newer initial data code, COCAL, has been developed by Uryū and Tsokaros [80], but not yet applied to BHNS binaries.

Our own group has developed an independent code ([25], henceforth Paper I) that uses a multidomain spectral method to achieve high accuracy at a relatively low computational

cost. The code is based on the spectral elliptic solver (Spells) developed by the Cornell-Caltech collaboration [81], and originally developed by Pfeiffer *et al.* [23, 82] for the study of binary black hole initial data. While the mathematical formulation of the problem is very similar to [76] and [77], the numerical techniques are quite different. In particular, while all use multidomain spectral methods, the flexibility that Spells offers in choosing subdomain shapes and the form of the elliptic equations allows one to efficiently adapt the configuration of the numerical grid to the geometry of the system and obtain high-precision results at a very reasonable computational cost.

A drawback of the method described in Paper I is that it fails to converge to a solution when the compactness $\mathcal{C}$ of the neutron star is too high. In fact, this seems to be a defect of all the published methods for solving the BHNS initial value problem. The maximum compactness that can be handled depends on the equation of state (EOS). The easiest EOS for all methods is a $\Gamma = 2$ polytrope because it is smooth inside the star, and the density goes linearly to zero near the surface. The method of Paper I can reliably produce binaries with an initial separation of $7M_0$ and a compactness up to 0.18. Here M_0 is defined via

$$M_0 = M_{\rm BH} + M_{\rm NS} \tag{3.2}$$

where $M_{\rm BH}$ is the Christodoulou mass of the black hole and $M_{\rm NS}$ is the neutron star mass as defined above. With some small modifications, described later, it can reach $\mathcal{C} = 0.20$, very close to the maximum allowed value before the neutron star is unstable to gravitational collapse.

Treating realistic equations of state is more difficult. They tend to have nonsmooth behavior as the composition changes in various density regimes. They often have nonanalytic behavior or very steep slopes at the surface. And even smooth equations of state may be given in tabular form, which introduces its own nonsmoothness. For example, for the SLy EOS [83–

85], the maximum compactness attainable by the method of Paper I is 0.16, corresponding to a neutron star mass of $1.27\,\mathrm{M}_\odot$. The other codes for producing BHNS initial data have reported a maximum compactness of $\mathcal{C} = 0.196$ with a piecewise-polytropic equation of state (for a $1.45 M_\odot$ neutron star) [86], while binary neutron star initial data has been obtained up to $\mathcal{C} = 0.213$ (for a $1.6 M_\odot$ neutron star) [65]. Since a neutron star of mass $2\,\mathrm{M}_\odot$ is known to exist, this is clearly not adequate.

In this paper, we describe several technical improvements to the algorithm of Paper I that allow high-compactness initial data to be calculated. For example, we show that for the SLy EOS, a solution with $\mathcal{C} = 0.25$, corresponding a neutron star mass of $1.86\,\mathrm{M}_\odot$, can be obtained. Furthermore, for the LS220 EOS [87], we can obtain a solution with $\mathcal{C} = 0.26$, corresponding to a mass of $1.98\,\mathrm{M}_\odot$. These initial data can now be used in binary evolutions to study the effect of high compactness on the outcome of the merger.

In [88], it was observed that highly compact configurations may result in mathematical nonuniqueness of the solution, and a resolution of this problem was presented in the context of conformally flat formulations for the evolution equations. In contrast, the work reported here is not related to nonuniqueness. Rather, we are dealing with an iterative algorithm that displays poor convergence as the compactness increases. The improvements to the algorithm restore good convergence.

In this paper, we first describe in section 3.2 the methods we use to improve the solution procedure of Paper I, in particular addressing requirements on the proper determination of the neutron star surface location and the control of linear momentum in the system. In section 3.3 we present high compactness results using polytropic, SLy, and LS220 EOS. Finally, in section 3.4 we offer closing remarks on these findings.

3.2 Methods

Our work is based on an implementation in the Spectral Einstein Code (SpEC) of the procedure described in Paper I. The core of the solution procedure is to solve a set of elliptic equations to determine the metric and the velocity potential for the matter (an "elliptic solve"). These elliptic equations contain a number of auxiliary variables that determine the physical properties of the initial data. Some of these are imposed based on analytical considerations, such as the background metric or boundary conditions, while others are solved for in between iterations in order to enforce desired physical properties (mass and spin of the compact objects, orbital parameters of the binary, total linear momentum of the system), or computationally convenient properties (alignment of the surface of the neutron star with the boundary between two subdomains). This procedure is described in detail in section III.C of Paper I.

In solving the elliptic equations, a relaxation scheme is used to keep the solution in a convergent regime. Instead of simply using the new solution at every step, it is combined with the previous one via

$$u_{\rm new} = \lambda u^* + (1-\lambda) u_{\rm old} \tag{3.3}$$

where λ is a parameter (the relaxation parameter) that we can choose, u is a quantity such as the value of the metric at some point, and u^* is the value of u found by solving the elliptic equations. This scheme decreases the change in the quantities at each step, which helps to maintain the convergence of the solver. In Paper I, we used $\lambda = 0.3$.

In this paper, we show that in order to obtain initial data for high-compactness neutron stars, modifications to the iterative procedure of Paper I are required. In particular, we need to modify how we enforce that the location of the surface of the neutron star is at a subdomain boundary and that the total linear ADM momentum of the system is zero.

3.2.1 Neutron Star Surface Adjustment

An important aspect of the solver is the numerical domain that is used to solve the equations. We employ the domain described in Paper I section III.A, and shown here in figure 3.1. The physical domain is covered by a number of overlapping spectral subdomains; choosing the location and resolution of the subdomains allows the domain to be well-matched to the problem. A particularly important detail (we have found) is that since the neutron star surface is a physical discontinuity, it should be placed at a subdomain boundary to avoid Gibbs oscillations in the numerical solution. This requirement was also found in Paper I, although we used a different technique to enforce it. We employ a modification of the method described in Paper I in section III.A.2 and in item 3 of the iterative procedure of section III.C.

We define the neutron star surface as the location where the enthalpy reaches some target value; the enthalpy h is defined via $h = 1 + \epsilon + P/\rho$, with ρ the baryon density, ϵ the internal energy density, and P the pressure. Note that in our code we assume beta-equilibrium and zero temperature, and so our choice for surface location is equivalent to letting it lie at constant pressure. However, we do not use the value $P = 0$. The reason is that tabulated equations of state have many discontinuous features at low density, and an extended low-density atmosphere. Trying to exactly capture those features in the same spectral subdomain as the core of the star significantly degrades the accuracy of the solution in high density regions. Instead we fix the surface at a constant non-zero pressure which is sufficiently low that only a small amount of matter is outside of that surface, and sufficiently high that many of the kinks in the low-density equation of state are in another subdomain. This choice defines the subdomain boundary and the location where we enforce the boundary condition on the velocity potential. The region outside this boundary is still permitted to contain matter, but the velocity flow is not irrotational.

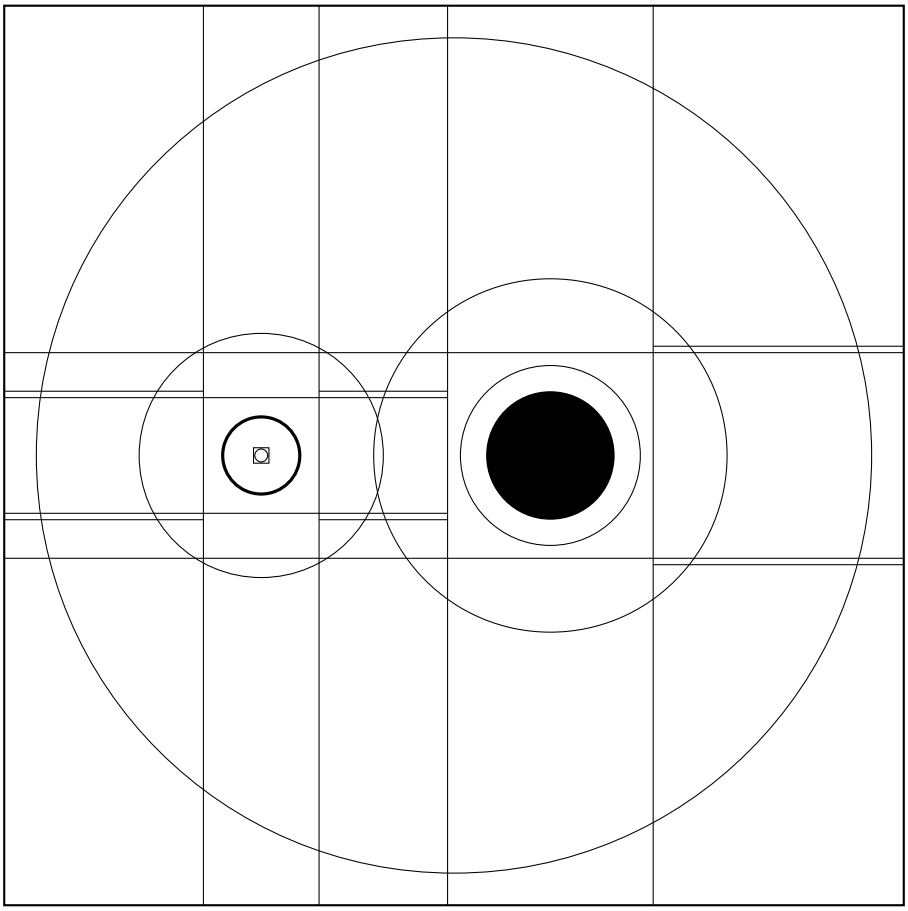

Figure 3.1: The domain used for the binary black hole–neutron star system. The horizon of the black hole is an external boundary of the domain; its interior is excised. The thick line shows the star surface; this and all other interior lines form subdomain boundaries. The largest circle is the inner boundary of the outer subdomain, this and all circles show the boundaries of spherical shells. The domain furthermore comprises eight cylindrical shells, in two stacked groups of five and three, and three rectangular prisms between and beside the objects.

In practice, the enthalpy is computed from the metric and the fluid velocity by assuming hydrostatic equilibrium (see Paper I). Since the neutron star surface may deviate slightly from the subdomain boundary during the solution, the equation for h is solved outside the star as well as inside. In principle, the enthalpy should take on a constant value everywhere in the vacuum region, but numerically h is allowed to take values below $h(\rho = 0)$, which ensures better behavior in the surface-finding algorithm. Similarly, the baryon density ρ is allowed to take unphysical values $\rho < 0$ in regions in which $h < h(\rho = 0)$ to guarantee that $\nabla\rho$ is continuous—a desirable property when using spectral methods.

The location of the surface can be found with a simple one-dimensional root finding algorithm along the collocation directions, which lets us find the stellar radius $R(\theta, \phi)$ as a function of angle. This is then used to define the stellar surface coefficients via an expansion in scalar spherical harmonics:

$$R(\theta, \phi) = \sum_{l} \sum_{m=-l}^{l} R_{lm} Y_l^m(\theta, \phi) \ . \tag{3.4}$$

Note that for $m \neq 0$, the coefficients R_{lm} will be complex-valued in general, but because $R(\theta, \phi)$ is real-valued, $R_{l,-m} = (-1)^m (R_{lm})^\star$ and so we can define

$$S_{lm} = \begin{cases} (-1)^m \sqrt{\frac{2}{\pi}}\, \mathrm{Re}(R_{lm}) & m \geq 0 \\ (-1)^m \sqrt{\frac{2}{\pi}}\, \mathrm{Im}(R_{lm}) & m < 0 \end{cases} \tag{3.5}$$

to store all independent components of the R_{lm} coefficients.

The coefficients in (3.5) are used to update the domain boundary for the neutron star subdomains used by the solver. However, since the enthalpy may have non-negligible errors early in the solve, the computed surface may not be in the right place and may have large jumps between iterations. This is similar to the difficulties that are encountered in the elliptic

solve. Accordingly, we follow a relaxation scheme as in (3.3) in updating the S_{lm} coefficients defined in (3.5), which are computed in each step and used to define the mapping shown in (77) and (78) in Paper I. We have found that choosing the same value for this relaxation parameter as for the one controlling the metric and matter relaxation gives good results.

3.2.2 ADM Momentum Control

To uniquely specify the initial conditions that we are attempting to produce, we need to fix the location of the centers of the black hole and neutron star, $\mathbf{c}_{\rm BH}$ and $\mathbf{c}_{\rm NS}$, the initial orbital angular velocity of the binary Ω_0, and its radial velocity $v_r = \dot{a}_0 r$. We also have the freedom to choose the value of the shift vector on the outer boundary of the computational domain, $\beta(r_{\rm out}) = \mathbf{v}^{\rm boost}$. We try to make these choices so that

- The linear ADM momentum of the system in the center-of-mass frame satisfies $\mathbf{P}^{\rm ADM} = 0$.
- The objects are following circular orbits with the desired initial separation d.
- The center of mass of the system is at the origin of the chosen coordinate system.

The initial data solver finds constraint-satisfying configurations by following the iterative procedure described in section III.C of Paper I. The center of the neutron star is fixed at $\mathbf{c}_{\rm NS} = (-d\, M_{\rm BH}/M_0, 0, 0)$. The quantities Ω_0 and $\dot{a}_0$ are chosen in order to minimize the orbital eccentricity of the system, following the iterative procedure developed for black hole–black hole binaries [89]. Alternatively, we can solve for Ω_0 by requiring force balance at the center of the neutron star, following (48) in Paper I as in step 5 of the iterative method described in section III.C of Paper I. Combined with the choice $\dot{a}_0 = 0$, this leads to eccentricities of a few percent, and provides a good initial guess for the eccentricity reduction algorithm. This leaves us with the choices of $\mathbf{c}_{\rm BH}$ and $\mathbf{v}^{\rm boost}$, which are both made iteratively. The location of the black hole center can be modified at each step of the iteration, after we

solve the constraint equations and evaluate the position of the neutron star surface (step 4 of the iterative procedure in Paper I). The choice of $\mathbf{v}^{\rm boost}$ comes as an outer boundary condition in the constraint equation for the shift. We have developed two different methods to choose $\mathbf{c}_{\rm BH}$ and $\mathbf{v}^{\rm boost}$.

The first (hereafter "position control") is largely similar to the algorithm described in Paper I for spin-aligned binaries, and updated in [90] for black hole spins misaligned with the orbital angular momentum of the binary. In this method, $\mathbf{c}_{\rm BH}$ is initialized to $\mathbf{c}^0_{\rm BH} = (d\,M_{\rm NS}/M, 0, 0)$. At each step n of the iterative procedure, we measure the linear ADM momentum $\mathbf{P}_n$, and the relative changes in each component $\delta P^i = |P^i_n - P^i_{n-1}|/|P^i_n|$. If $\delta P^i < \alpha_P$ for the largest component P^i_n of the ADM momentum and a freely specifiable parameter α_P, then we reset the components of $\mathbf{c}_{\rm BH}$ in the orbital plane of the binary (the x-y plane here) using the relaxation formula

$$c^{\rm new}_{x,y} = \lambda_P c^*_{x,y} + (1-\lambda_P) c^{\rm old}_{x,y} \tag{3.6}$$

analogously to (3.3), with $c^*_{x,y}$ computed using the values of $P^{x,y}$ and $c_{x,y}$ at the two latest steps i and j at which the location of the black hole center was modified:

$$c^*_{x,y} = \frac{c^i_{x,y} P^{y,x}_j - c^j_{x,y} P^{y,x}_i}{P^{y,x}_j - P^{y,x}_i}. \tag{3.7}$$

For larger neutron stars, we have been using $\alpha_P = 0.1$, $\lambda_P = 1$. For compact stars, we find that changing the location of the black hole center more often, but by smaller increments, works better. Accordingly, we use $\alpha_P = 0.4$, and λ_P is chosen to equal the relaxation parameter in the elliptic solve. Equation (3.7) is inspired by the fact that, in Newtonian physics, a change $\delta\mathbf{c}$ in $\mathbf{c}_{\rm BH}$ induces a change $\delta\mathbf{P} = -\delta\mathbf{c} \times \mathbf{\Omega}$ in $\mathbf{P}$. A similar updating algorithm is used for the vertical location of the black hole center, except that instead of trying to cancel the linear momentum of the system, we require vertical force balance

$(\nabla h)_z = 0$ at the center of the neutron star. Thus we use

$$c_z^* = \frac{c_z^i (\nabla h)_z^j - c_z^j (\nabla h)_z^i}{(\nabla h)_z^j - (\nabla h)_z^i}. \tag{3.8}$$

The vertical component of the linear momentum, which cannot be easily controlled by moving the location of the compact objects, is instead canceled by a "boost" given to the entire system through the chosen value $\mathbf{v}^{\rm boost}$ of the shift on the outer boundary. We set $v_{x,y}^{\rm boost} = 0$ and update $v_z^{\rm boost}$ using the same method as for the black hole center, but with

$$v_z^* = \frac{v_z^i P_j^z - v_z^j P_i^z}{P_j^z - P_i^z}. \tag{3.9}$$

In the second method (hereafter "boost control"), the location of the center of the black hole is fixed to its expected value for a Newtonian binary orbiting around the origin of our coordinate system, $\mathbf{c}_{\rm BH} = (d\, M_{\rm NS}/M, 0, 0)$. The constraint $\mathbf{P}^{\rm ADM} = 0$ is then satisfied by controlling all components of the linear momentum through the outer boundary condition on the shift. That is, we use

$$v_{x,y,z}^* = \frac{v_{x,y,z}^i P_j^{x,y,z} - v_{x,y,z}^j P_i^{x,y,z}}{P_j^{x,y,z} - P_i^{x,y,z}} \tag{3.10}$$

to reset the components of $\mathbf{v}^{\rm boost}$ whenever $\delta P^i < \alpha_P$.

For spin-aligned binaries, position control generally results in a very small coordinate velocity for the center of mass of the system. On the other hand, imposing a non-zero boundary condition on the shift at large distances leads to a drift of the coordinate location of the center of mass at velocity $v^{\rm COM} \sim v^{\rm boost}$. This effect was observed for misaligned BHNS binaries in [90]. Because a large drift of the center of mass might introduce undesirable coordinate effects in the methods used to extrapolate the gravitational wave signal to infinity, or complicate the work of the control system used to evolve the binary in the comoving frame,

we have generally preferred position control. However, each change of the location of the center of the black hole in the initial data solver introduces significant constraint violations in our solution. We find that, for very compact stars with $\mathcal{C} \gtrsim 0.2$, these changes can prevent convergence of the iterative procedure used to generate initial data, and so we avoid position control in these cases.

3.3 Results

Using the methods described above, we were able to obtain solutions for binaries with various neutron star compactness for a variety of different equations of state. In all cases, we have chosen the black hole to be nonspinning, since the aim of the study was to develop methods for handling high neutron star compactness.

3.3.1 Polytropic $\Gamma = 2$ EOS

Using the methods of Paper I, tweaking only the elliptic solve relaxation parameter described in the iterative procedure in section III.C, solutions for polytropic $\Gamma = 2$ equations of state with compactness up to 0.18 could be obtained. If we additionally incorporate an initial guess based on a lower-compactness binary instead of starting with an isolated neutron star configuration, a solution with $\mathcal{C} = 0.20$ could be found. Finally, using the techniques described in section 3.2, we are able to obtain solutions with compactness up to $\mathcal{C} = 0.21$ and mass of $1.4\,\mathrm{M}_\odot$. For the family of equations of state we consider, there is a dynamic instability that sets in for compactness slightly higher than 0.21, and so this is roughly the highest compactness that we expect to be physically meaningful. In addition, other work [88] has found mathematical nonuniqueness problems with obtaining solutions for stars that are dynamically unstable, and for both these reasons we avoid investigating such solutions. For polytropes, we could thus nearly reach the maximum stable compactness without further modifications of the elliptic solve. Only the highest stable compactness $\mathcal{C} = 0.21$ still required

the techniques introduced above. By contrast, for the SLy and LS220 equations of state, the methods of Paper I fail at much lower compactness.

We show in table 3.1 the results for applying this method to $\Gamma = 2$ polytropes of different compactness. The stellar mass is held constant at $1.4\,\mathrm{M}_\odot$ and so the polytropic parameter κ varies across these solutions and is included in the table. (Note that for polytropes, the mass can be rescaled by changing κ without affecting $\mathcal{C}$.) The mass ratio is 6:1 for all cases. The binding energy E_b is computed by subtracting the sum of the ADM masses of the black hole and neutron star in isolation from the ADM energy of the system. The surface coefficients shown are defined in (3.5). The residuals obtained as a function of resolution are shown in figure 3.2. In the residuals we can see some aberrant behavior and jumps, but nevertheless the exponential convergence with resolution that characterizes spectral methods is apparent, especially if one focuses on the higher resolutions. The convergence with resolution also does not seem to vary among the different cases, so that compactness does not seem to be an issue here. One other thing to note here is that the initial distance d between the black hole and neutron star is chosen to be quite close in all but the highest compactness cases, as compared with the values in tables 2, 5, and 6 in Paper I.

3.3.2 SLy EOS

Using the methods of this paper, we can obtain solutions for an SLy equation of state with compactness up to $\mathcal{C} = 0.25$, which corresponds to a star with a mass of $1.86\,\mathrm{M}_\odot$. For comparison, the maximum stable compactness for this equation of state is about $\mathcal{C} = 0.31$, corresponding to a mass of $2.04\,\mathrm{M}_\odot$. Solutions were found for a variety of different distances, although as the compactness becomes greater, it becomes more difficult to obtain solutions for very close binaries. At the highest compactness, the closest binaries we attempted did not have a convergent solution, and so an evolution of such a system would need to simulate more than 20 orbits before a merger.

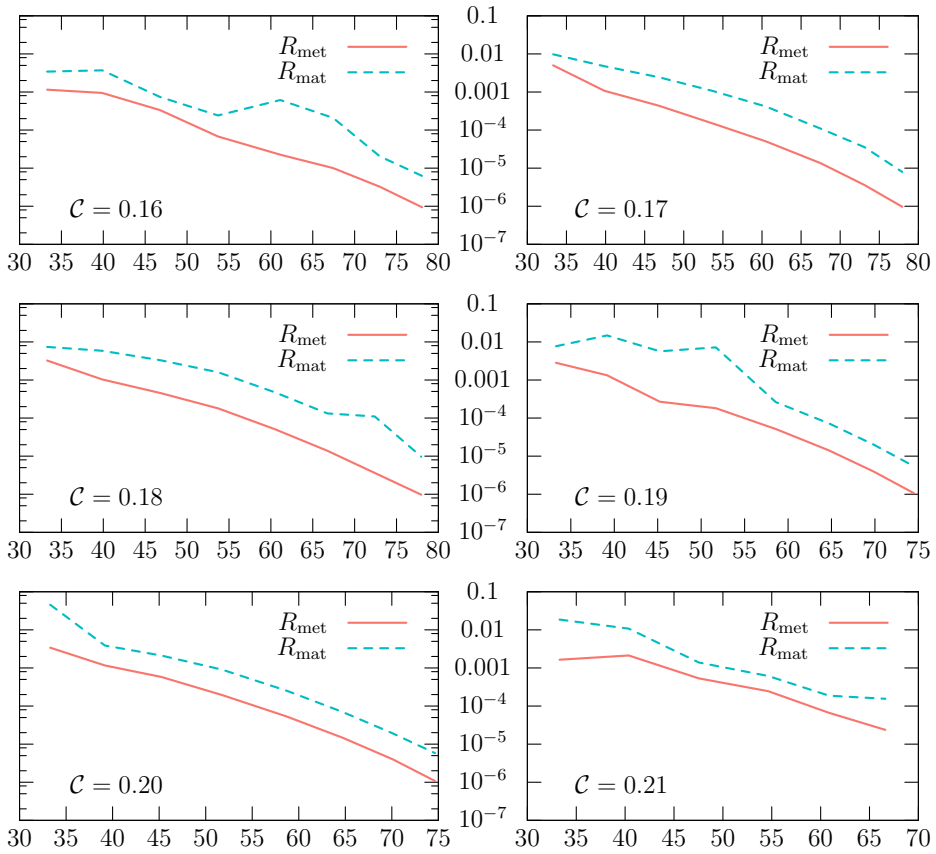

Figure 3.2: Spectral convergence for a family of BHNS binary configurations. For each configuration, the equation of state is a $\Gamma = 2$ polytrope chosen to yield $M_{\rm NS} = 1.4\,{\rm M}_\odot$. Each panel shows the final residual in the metric solution ($R_{\rm met}$) and in the velocity potential solution ($R_{\rm mat}$) as a function of the cube root of the number of grid points in the domain. The vertical scale is logarithmic, and the exponential convergence with resolution is apparent.

$\mathcal{C}$	κ	λ	d/M_0	ΩM_0	E_b/M_0	$J/{M_0}^2$	S_{20}/S_{00}
0.15	96.7	0.3	6.86	0.046 48	−6.69	0.422	4.261
0.16	89.7	0.3	6.86	0.046 49	−6.70	0.421	4.439
0.17	84.1	0.2	6.86	0.046 50	−6.71	0.421	4.474
0.18	79.8	0.2	6.86	0.046 50	−6.71	0.421	4.412
0.19	76.6	0.2	7.71	0.039 67	−6.19	0.434	3.574
0.20	74.4	0.2	7.71	0.039 68	−6.19	0.434	3.419
0.21	73.2	0.15	14.0	0.017 40	−3.85	0.526	1.441
					$\times 10^{-3}$		$\times 10^{-3}$

Table 3.1: Solved quantities for a family of BHNS binary configurations. For each configuration, the equation of state is a $\Gamma = 2$ polytrope chosen to yield $M_{\rm NS} = 1.4\,{\rm M}_\odot$. The multiplier below applies to the column above it. The columns show the compactness $\mathcal{C}$, the polytropic parameter κ, the relaxation parameter λ, the initial separation d, the orbital angular velocity Ω, the binding energy E_b, the ADM angular momentum J, and the ratio S_{20}/S_{00} of surface coefficients defined in (3.5). The quantity M_0 is defined in (3.2). In all cases the black hole has no spin and the mass ratio is 6:1.

These results are shown in table 3.2. The mass ratio q is close to 6, with slight variations between solutions. The residuals obtained in the solve are shown in figure 3.3, plotted against $N^{1/3}$, the cube root of the number of points in the domain. Note that for the $\mathcal{C} = 0.23$ and $\mathcal{C} = 0.25$ cases, we have only plotted the convergence in the case of $d = 14M_0$. Even more so than in the polytropic case, there are some jumps in the residuals, particularly in the velocity potential. Furthermore, jumps are present at all compactnesses instead of just low ones. However, once again, the convergence does appear smoothly exponential at high resolution. The same value for the relaxation parameter is used for all of the various quantities that are updated via a relaxation scheme.

3.3.3 LS220 EOS

We obtain solutions for an LS220 tabulated equation of state with compactness up to $\mathcal{C} = 0.26$, which corresponds to a star with a mass of $1.98\,{\rm M}_\odot$. For comparison, the largest known reliable neutron star masses are $(1.97 \pm 0.04)\,{\rm M}_\odot$ [8] and $(2.01 \pm 0.04)\,{\rm M}_\odot$ [91]. The LS220 equation of state is the most realistic of the ones considered here, and so this is a very relevant

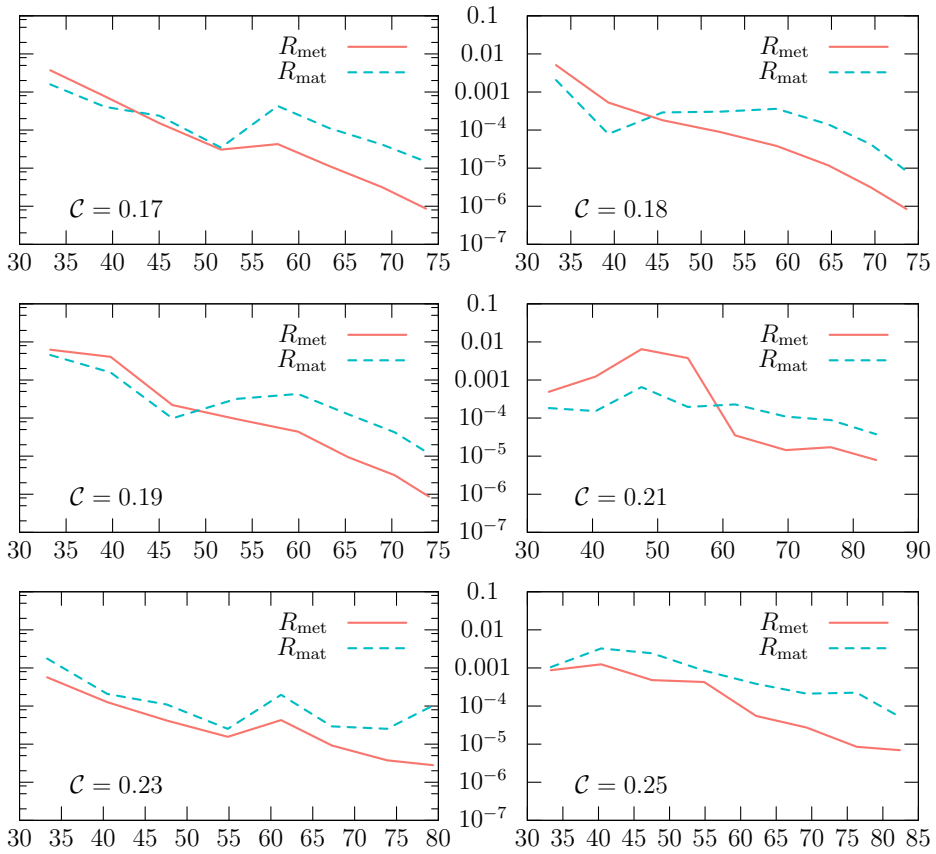

Figure 3.3: Spectral convergence for a family of BHNS binary configurations. For each configuration, the equation of state is SLy. Each panel shows the final residual in the metric solution ($R_{\rm met}$) and in the velocity potential solution ($R_{\rm mat}$) as a function of the cube root of the number of grid points in the domain. The vertical scale is logarithmic, and the exponential convergence with resolution is apparent.

$\mathcal{C}$	$M_{\rm NS}$	q	λ	d/M_0	ΩM_0	E_b/M_0	$J/{M_0}^2$	S_{20}/S_{00}
0.16	1.27	6.64	0.2	6.95	0.045 60	−6.15	0.393	4.928
0.17	1.34	6.26	0.2	6.90	0.046 11	−6.46	0.409	4.696
0.18	1.41	5.94	0.2	6.85	0.046 59	−6.77	0.424	4.460
0.19	1.49	5.65	0.2	6.80	0.047 07	−7.05	0.438	4.231
0.21	1.62	6.0	0.15	13.71	0.017 91	−3.91	0.522	1.533
0.23	1.75	6.0	0.15	8.0	0.037 85	−6.05	0.438	2.878
0.23	1.75	6.0	0.15	10.0	0.027 85	−5.09	0.468	2.066
0.23	1.75	6.0	0.15	12.0	0.021 60	−4.39	0.497	1.611
0.23	1.75	6.0	0.15	14.0	0.017 39	−3.82	0.526	1.324
0.23	1.75	6.0	0.15	16.0	0.014 39	−3.22	0.552	1.124
0.25	1.86	6.0	0.1	14.0	0.017 38	−3.88	0.525	1.144
0.25	1.86	6.0	0.1	16.0	0.014 38	−2.38	0.552	0.971
						$\times 10^{-3}$		$\times 10^{-3}$

Table 3.2: Solved quantities for a family of BHNS binary configurations. For each configuration, the equation of state is SLy. The multiplier below applies to the column above it. The quantities shown are all as for table 3.1, with κ replaced by the neutron star ADM mass $M_{\rm NS}$ in units of $M_\odot$. We also show the mass ratio q for each configuration.

result. The largest compactness for which this equation of state yields a stable solution is $\mathcal{C} = 0.29$, corresponding to a mass of $2.04\,\mathrm{M}_\odot$.

These results are shown in table 3.3. In all cases, the mass ratio is 6:1. The residuals obtained in the solve are shown in figure 3.4, plotted against $N^{1/3}$, the cube root of the number of points in the domain. As before, we find exponential convergence, and obtain a final residual of 10^{-5} or better.

It is worth briefly discussing the differences in final residuals among the various solutions we obtain. Comparing the various cases, we find a solution for the metric quantities and velocity potential whose residual is worse for the most compact solutions than the least compact ones by about a factor of 10. Generally speaking, the metric residual reaches 10^{-5} in the worst cases and the velocity potential reaches 10^{-4}. We consider this to be a suitable result for the purpose of evolving these systems through merger. We performed a very short examination of the behavior of our most compact LS220 solution in an evolution, and found that the convergence of the constraints and their values are quite acceptable, similar to what

$\mathcal{C}$	$M_{\rm NS}$	λ	d/M_0	ΩM_0	E_b/M_0	$J/{M_0}^2$	S_{20}/S_{00}
0.17	1.40	0.2	14.0	0.017 39	−3.84	0.526	1.885
0.23	1.83	0.1	14.0	0.017 39	−3.83	0.526	1.347
0.25	1.94	0.08	16.0	0.014 39	−3.18	0.552	0.985
0.26	1.98	0.07	14.0	0.017 39	−3.73	0.525	1.075
					$\times 10^{-3}$		$\times 10^{-3}$

Table 3.3: Solved quantities for a family of BHNS binary configurations. For each configuration, the equation of state is the LS220 tabulated equation of state. The multiplier below applies to the column above it. The quantities shown are all as for table 3.1, with κ replaced by the neutron star ADM mass $M_{\rm NS}$ in units of $M_\odot$.

is seen with a much less compact star. In terms of matter, we see an initial anomaly in the density larger than in the low compactness case, but this anomaly decreases with resolution.

3.4 Conclusions

The problem of solving for initial data for a black hole–neutron star system is a complex one involving many interacting solution steps. In addition to the elliptic equations governing the system, multiple nonlinear constraints must be imposed simultaneously. In this paper, we focused on two of these in particular: aligning the surface with a subdomain boundary and enforcing zero linear momentum on the binary system. The close interaction between the equations and all of the constraints requires care in solving the system, and for some choices of system parameters the convergence of the system can be very sensitive to deficiencies in the solution method. In fact, it seems to be generally true that high compactness stars cause difficulty with the various solvers that exist.

We have found that by applying additional relaxation steps to the method of Paper I [25] we could obtain solutions for a wide variety of systems with quite high compactness stars, including stars with polytropic, SLy, and LS220 equations of state. This includes a solution for a binary with a physically realistic LS220 equation of state star having a mass of $M = 1.98\,\mathrm{M}_\odot$. We have found it effective to employ a relaxation scheme in updating

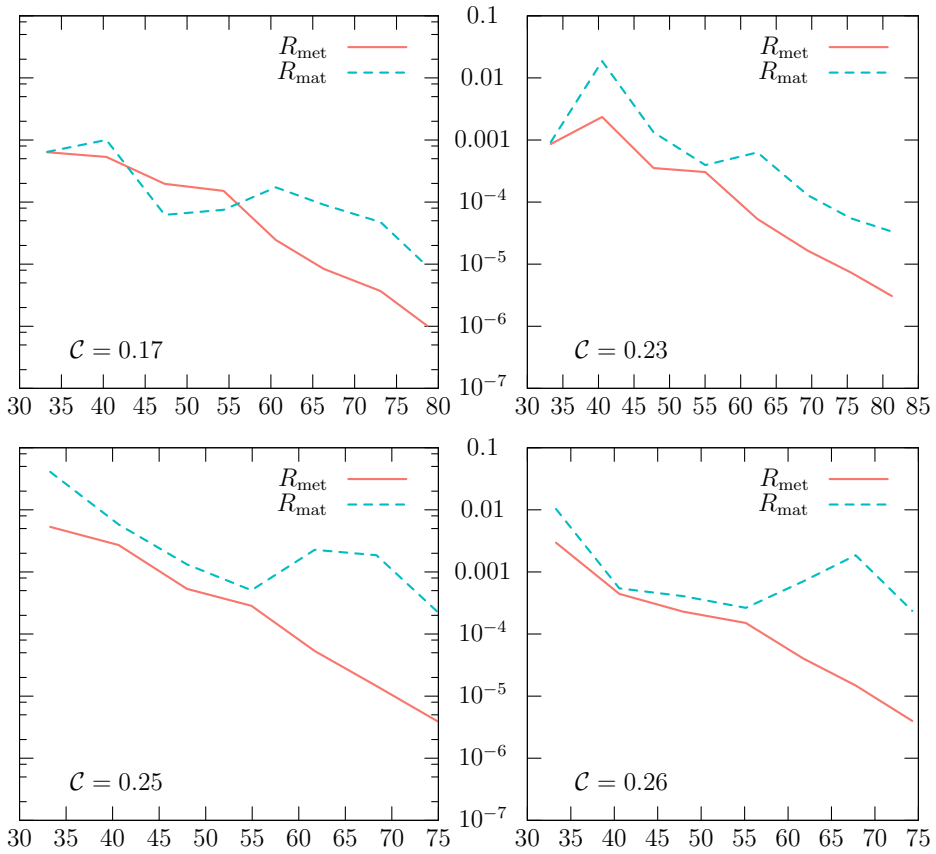

Figure 3.4: Spectral convergence for a family of BHNS binary configurations. For each configuration, the equation of state is LS220. Each panel shows the final residual in the metric solution ($R_{\rm met}$) and in the velocity potential solution ($R_{\rm mat}$) as a function of the cube root of the number of grid points in the domain. The vertical scale is logarithmic, and the exponential convergence with resolution is apparent.

the metric and velocity potential quantities from the elliptic solver procedure, as well as the neutron star surface location, in addition to a boost parameter in a control scheme adjusting for undesired linear ADM momentum in the system. The choice of different relaxation parameters allows one to tune the solver for the convergence properties of the particular solution being examined. These improvements allow solutions to the black hole–neutron star initial data problem to be found for physically important cases.

Acknowledgements

K.H. would like to thank Geoffrey Lovelace, Curran Muhlberger, Harald Pfeiffer, and David Chernoff for useful discussions, and Andy Bohn for the use of computing resources. This work was supported in part by NSF Grants PHY-1306125 and AST-1333129 at Cornell University, and by a grant from the Sherman Fairchild Foundation. F.F. gratefully acknowledges support from the Vincent and Beatrice Tremaine Postdoctoral Fellowship and NSERC Canada. Support for this work was provided by NASA through Einstein Postdoctoral Fellowship grant number PF4-150122 awarded by the Chandra X-ray Center, which is operated by the Smithsonian Astrophysical Observatory for NASA under contract NAS8-03060. This research was performed in part using the Zwicky computer system operated by the Caltech Center for Advanced Computing Research and funded by NSF MRI No. PHY-0960291 and the Sherman Fairchild Foundation.

Bibliography

[1] Baym, G., Pethick, C., and Pines, D.: 1969, *Nature* **224(5220)**, 673

[2] Easson, I. and Pethick, C. J.: 1977, *Phys. Rev. D* **16(2)**, 275

[3] Zuo, W., Cui, C. X., Lombardo, U., and Schulze, H.-J.: 2008, *Phys. Rev. C* **78(1)**, 015805

[4] Zuo, W., Li, Z., Lu, G., Li, J., Scheid, W., Lombardo, U., Schulze, H.-J., and Shen, C.: 2004, *Phys. Lett. B* **595**, 44

[5] Flowers, E., Ruderman, M., and Sutherland, P.: 1976, *Astrophys. J.* **205**, 541

[6] Shternin, P. S., Yakovlev, D. G., Heinke, C. O., Ho, W. C. G., and Patnaude, D. J.: 2011, *Mon. Not. R. Astron. Soc.* **412(1)**, L108

[7] Page, D., Prakash, M., Lattimer, J. M., and Steiner, A. W.: 2011, *Phys. Rev. Lett.* **106(8)**, 081101

[8] Demorest, P., Pennucci, T., Ransom, S., Roberts, M., and Hessels, J.: 2010, *Nature* **467(7319)**, 1081

[9] Monaghan, J. J. and Roxburgh, I. W.: 1965, *Mon. Not. R. Astron. Soc.* **131(1)**, 105

[10] Roberts, P. H.: 1981, *Q. J. Mech. Appl. Math.* **34(3)**, 327

[11] Akgün, T. and Wasserman, I.: 2008, *Mon. Not. R. Astron. Soc.* **383(4)**, 1551

[12] Akgün, T.: 2007, *Ph.D. thesis*, Cornell University

[13] Lander, S. K., Andersson, N., and Glampedakis, K.: 2012, *Mon. Not. R. Astron. Soc.* **419(1)**, 732

[14] Harry, G. M. and the LIGO Scientific Collaboration: 2010, *Class. Quantum Grav.* **27(8)**, 084006

[15] Abadie, J., Abbott, B. P., Abbott, R., Abernathy, M., Accadia, T., Acernese, F., Adams, C., Adhikari, R., Ajith, P., Allen, B., Allen, G., Ceron, E. A., Amin, R. S., Anderson, S. B., Anderson, W. G., Antonucci, F., *et al.*: 2010, *Class. Quantum Grav.* **27(17)**, 173001

[16] Pretorius, F.: 2005, *Phys. Rev. Lett.* **95(12)**, 121101

[17] Baumgarte, T. and Shapiro, S.: 2010, *Numerical Relativity: Solving Einstein's Equations on the Computer*, Cambridge University Press

[18] Duez, M. D.: 2010, *Class. Quantum Grav.* **27(11)**, 114002

[19] Faber, J. A. and Rasio, F. A.: 2012, *Living Rev. Relat.* **15(8)**, 8

[20] Teukolsky, S. A.: 1998, *Astrophys. J.* **504(1)**, 442

[21] Shibata, M.: 1998, *Phys. Rev. D* **58(2)**, 024012

[22] Grandclément, P., Gourgoulhon, E., and Bonazzola, S.: 2002, *Phys. Rev. D* **65(4)**, 044021

[23] Pfeiffer, H. P., Kidder, L. E., Scheel, M. A., and Teukolsky, S. A.: 2003, *Comput. Phys. Commun.* **152(3)**, 253

[24] Gourgoulhon, E., Grandclément, P., Taniguchi, K., Marck, J.-A., and Bonazzola, S.: 2001, *Phys. Rev. D* **63(6)**, 064029

[25] Foucart, F., Kidder, L. E., Pfeiffer, H. P., and Teukolsky, S. A.: 2008, *Phys. Rev. D* **77(12)**, 124051

[26] Press, W. H., Teukolsky, S. A., Vetterling, W. T., and Flannery, B. P.: 2007, *Numerical Recipes 3rd Edition: The Art of Scientific Computing*, Cambridge University Press

[27] Hesthaven, J., Gottlieb, S., and Gottlieb, D.: 2007, *Spectral Methods for Time-Dependent Problems*, Cambridge Monographs on Applied and Computational Mathematics, Cambridge University Press

[28] Canuto, C., Hussaini, M., Quarteroni, A., and Zang, T.: 1988, *Spectral Methods in Fluid Dynamics*, Computational Physics Series, Springer-Verlag

[29] Boyd, J.: 2013, *Chebyshev and Fourier Spectral Methods: Second Revised Edition*, Dover Books on Mathematics, Dover Publications

[30] Fornberg, B.: 1998, *A Practical Guide to Pseudospectral Methods*, Cambridge Monographs on Applied and Computational Mathematics, Cambridge University Press

[31] Andreev, A. F. and Bashkin, E. P.: 1976, *Sov. Phys. JETP* **42**, 164

[32] Alpar, M. A., Langer, S. A., and Sauls, J. A.: 1984, *Astrophys. J.* **282**, 533

[33] Sedrakian, A. D. and Sedrakian, D. M.: 1995, *Astrophys. J.* **447**, 305

[34] Zuo, W.: 2013, *J. Phys. Conf. Ser.* **420(1)**, 012089

[35] Baym, G., Bethe, H. A., and Pethick, C. J.: 1971, *Nucl. Phys. A* **175(2)**, 225

[36] Haensel, P.: 2001, in D. Blaschke, N. K. Glendenning, and A. Sedrakian (eds.), *Physics of Neutron Star Interiors*, Vol. 578 of *Lecture Notes in Physics, Berlin Springer Verlag*, p. 127

[37] Hebeler, K., Schwenk, A., and Friman, B.: 2007, *Phys. Lett. B* **648**, 176

[38] Blandford, R. D., Applegate, J. H., and Hernquist, L.: 1983, *Mon. Not. R. Astron. Soc.* **204(4)**, 1025

[39] Pons, J. A., Miralles, J. A., and Geppert, U.: 2009, *Astron. Astrophys.* **496(1)**, 207

[40] Wentzel, D. G.: 1961, *Astrophys. J.* **133**, 170

[41] Prendergast, K. H.: 1956, *Astrophys. J.* **123**, 498

[42] Mastrano, A., Melatos, A., Reisenegger, A., and Akgün, T.: 2011, *Mon. Not. R. Astron. Soc.* **417(3)**, 2288

[43] Woltjer, L.: 1960, *Astrophys. J.* **131**, 227

[44] Lander, S. K.: 2013, *Phys. Rev. Lett.* **110(7)**, 071101

[45] Wright, G. A. E.: 1973, *Mon. Not. R. Astron. Soc.* **162(4)**, 339

[46] Markey, P. and Tayler, R. J.: 1973, *Mon. Not. R. Astron. Soc.* **163(1)**, 77

[47] Horowitz, C. J. and Kadau, K.: 2009, *Phys. Rev. Lett.* **102(19)**, 191102

[48] Baiko, D. A.: 2011, *Mon. Not. R. Astron. Soc.* **416(1)**, 22

[49] Lorimer, D. R. and Kramer, M.: 2012, *Handbook of Pulsar Astronomy*, Cambridge University Press

[50] Muzikar, P. and Pethick, C. J.: 1981, *Phys. Rev. B* **24(5)**, 2533

[51] Andersson, N., Comer, G., and Glampedakis, K.: 2005, *Nucl. Phys. A* **763**, 212

[52] Eichler, D., Livio, M., Piran, T., and Schramm, D. N.: 1989, *Nature* **340**, 126

[53] Narayan, R., Paczynski, B., and Piran, T.: 1992, *Astrophys. J. Lett.* **395**, L83

[54] Mochkovitch, R., Hernanz, M., Isern, J., and Martin, X.: 1993, *Nature* **361**, 236

[55] Lee, W. H. and Kluźniak, W.: 1998, in C. A. Meegan, R. D. Preece, & T. M. Koshut (ed.), *Gamma-Ray Bursts, 4th Hunstville Symposium*, Vol. 428 of *American Institute of Physics Conference Series*, p. 798

[56] Janka, H.-T., Eberl, T., Ruffert, M., and Fryer, C. L.: 1999, *Astrophys. J. Lett.* **527(1)**, L39

[57] Roberts, L. F., Kasen, D., Lee, W. H., and Ramirez-Ruiz, E.: 2011, *Astrophys. J. Lett.* **736(1)**, L21

[58] Metzger, B. D. and Berger, E.: 2012, *Astrophys. J.* **746(1)**, 48

[59] Tanaka, M., Hotokezaka, K., Kyutoku, K., Wanajo, S., Kiuchi, K., Sekiguchi, Y., and Shibata, M.: 2014, *Astrophys. J.* **780(1)**, 31

[60] Foucart, F., Deaton, M. B., Duez, M. D., Kidder, L. E., MacDonald, I., Ott, C. D., Pfeiffer, H. P., Scheel, M. A., Szilágyi, B., and Teukolsky, S. A.: 2013, *Phys. Rev. D* **87(8)**, 084006

[61] Kyutoku, K., Ioka, K., and Shibata, M.: 2013, *Phys. Rev. D* **88(4)**, 041503

[62] Lovelace, G., Duez, M. D., Foucart, F., Kidder, L. E., Pfeiffer, H. P., Scheel, M. A., and Szilágyi, B.: 2013, *Class. Quantum Grav.* **30(13)**, 135004

[63] Deaton, M. B., Duez, M. D., Foucart, F., O'Connor, E., Ott, C. D., Kidder, L. E., Muhlberger, C. D., Scheel, M. A., and Szilágyi, B.: 2013, *Astrophys. J.* **776(1)**, 47

[64] Foucart, F., Deaton, M. B., Duez, M. D., O'Connor, E., Ott, C. D., Haas, R., Kidder, L. E., Pfeiffer, H. P., Scheel, M. A., and Szilágyi, B.: 2014, *Phys. Rev. D* **90(2)**, 024026

[65] Hotokezaka, K., Kiuchi, K., Kyutoku, K., Okawa, H., Sekiguchi, Y.-i., Shibata, M., and Taniguchi, K.: 2013, *Phys. Rev. D* **87(2)**, 024001

[66] Finn, L. S.: 1992, *Phys. Rev. D* **46(12)**, 5236

[67] Finn, L. S. and Chernoff, D. F.: 1993, *Phys. Rev. D* **47(6)**, 2198

[68] Abadie, J., Abbott, B. P., Abbott, R., Abernathy, M., Accadia, T., Acernese, F., Adams, C., Adhikari, R., Ajith, P., Allen, B., Allen, G. S., Amador Ceron, E., Amin, R. S., Anderson, S. B., Anderson, W. G., Antonucci, F., *et al.*: 2011, *Phys. Rev. D* **83(12)**, 122005

[69] Babak, S., Biswas, R., Brady, P. R., Brown, D. A., Cannon, K., Capano, C. D., Clayton, J. H., Cokelaer, T., Creighton, J. D. E., Dent, T., Dietz, A., Fairhurst, S., Fotopoulos, N., González, G., Hanna, C., Harry, I. W., *et al.*: 2013, *Phys. Rev. D* **87(2)**, 024033

[70] Shibata, M. and Taniguchi, K.: 2011, *Living Rev. Relat.* **14(6)**, 6

[71] Lehner, L. and Pretorius, F.: 2014, *Annu. Rev. Astron. Astrophys.* **52(1)**, 661

[72] Taniguchi, K., Baumgarte, T. W., Faber, J. A., and Shapiro, S. L.: 2005, *Phys. Rev. D* **72(4)**, 044008

[73] Sopuerta, C. F., Sperhake, U., and Laguna, P.: 2006, *Class. Quantum Grav.* **23(16)**, S579

[74] Taniguchi, K., Baumgarte, T. W., Faber, J. A., and Shapiro, S. L.: 2006, *Phys. Rev. D* **74(4)**, 041502

[75] Taniguchi, K., Baumgarte, T. W., Faber, J. A., and Shapiro, S. L.: 2007, *Phys. Rev. D* **75(8)**, 084005

[76] Taniguchi, K., Baumgarte, T. W., Faber, J. A., and Shapiro, S. L.: 2008, *Phys. Rev. D* **77(4)**, 044003

[77] Grandclément, P.: 2006, *Phys. Rev. D* **74(12)**, 124002

[78] Gourgoulhon, E., Grandclément, P., Marck, J.-A., and Novak, J.: 2012, *LORENE web page*, `http://www.lorene.obspm.fr/`

[79] Kyutoku, K., Shibata, M., and Taniguchi, K.: 2009, *Phys. Rev. D* **79(12)**, 124018

[80] Uryū, K. b. o. and Tsokaros, A.: 2012, *Phys. Rev. D* **85(6)**, 064014

[81] Pfeiffer, H. P. and York, J. W.: 2003, *Phys. Rev. D* **67(4)**, 044022

[82] Pfeiffer, H. P., Cook, G. B., and Teukolsky, S. A.: 2002, *Phys. Rev. D* **66(2)**, 024047

[83] F. Douchin and P. Haensel: 2001, *Astron. Astrophys.* **380(1)**, 151

[84] P. Haensel and A. Y. Potekhin: 2004, *Astron. Astrophys.* **428(1)**, 191

[85] Shibata, M., Taniguchi, K., and Uryū, K. b. o.: 2005, *Phys. Rev. D* **71(8)**, 084021

[86] Kyutoku, K., Okawa, H., Shibata, M., and Taniguchi, K.: 2011, *Phys. Rev. D* **84(6)**, 064018

[87] Lattimer, J. M. and Swesty, F. D.: 1991, *Nucl. Phys. A* **535(2)**, 331

[88] Cordero-Carrión, I., Cerdá-Durán, P., Dimmelmeier, H., Jaramillo, J. L., Novak, J., and Gourgoulhon, E.: 2009, *Phys. Rev. D* **79(2)**, 024017

[89] Pfeiffer, H. P., Brown, D. A., Kidder, L. E., Lindblom, L., Lovelace, G., and Scheel, M. A.: 2007, *Class. Quantum Grav.* **24(12)**, S59

[90] Foucart, F., Duez, M. D., Kidder, L. E., and Teukolsky, S. A.: 2011, *Phys. Rev. D* **83(2)**, 024005

[91] Antoniadis, J., Freire, P. C. C., Wex, N., Tauris, T. M., Lynch, R. S., van Kerkwijk, M. H., Kramer, M., Bassa, C., Dhillon, V. S., Driebe, T., Hessels, J. W. T., Kaspi, V. M., Kondratiev, V. I., Langer, N., Marsh, T. R., McLaughlin, M. A., *et al.*: 2013, *Science* **340(6131)**, 448